Strål
säkerhets
myndigheten
Swedish Radiation Safety Authority

Research

Warm Pre-Stressing mechanisms

2022:04

Author: Tobias Bolinder[1], Alexander Eriksson[1], Jonas Faleskog[2], Irene Linares Arregui[2], Martin Öberg[2], Bård Nyhus[3]
[1]Kiwa Technical Consulting AB, Stockholm, Sweden
[2]Royal Institute of Technology, Department of Solid Mechanics, Stockholm, Sweden
[3]SINTEF, Trondheim, Norway
Report number: 2020:04
ISSN: 2000-0456
Available at: www.ssm.se

SSM perspective

Background

Swedish nuclear power plants (NPP) were originally designed and analyzed with an assumed operating period of approximately 40 years. As Swedish NPPs reach their original technical design life the safety of the additional operating time has to be verified. With increased operating time, the shift in the fracture toughness curve of the reactor pressure vessel (RPV) must be accounted for in structural integrity assessments.

This project investigates the mechanisms that contribute to the apparent increase in fracture toughness of components with an assumed crack like defect, i.e Warm Pre-Stressing (WPS). WPS is a benificial effect that increases the fracture toughness of a component when certain conditions are met, e.g. the component is first preloaded in the ductile region after which it is cooled to the brittle fracture region. Upon reloading, fracture is expected to occur at higher loads than for virgin, unprestressed material.

The research was initiated by SSM and is relevant considering the aging reactor fleet in Sweden. The project is expected to provide answers to the applicability of the engineering methods currently applied to analyse the WPS effects. The project aims to provide insights for improved analytical approaches.

Results

An extensive fracture mechanic testing programme, where the effects of the contributing mechanisms were singled out and studied one-by-one showing that

- the most influential mechanism behind the WPS effect is the change in yield strength due to the lowering of the temperature,
- as long as the load is constant or monotonous declining during cooling, the actual load path can be considered path independent,
- the deactivation of initiation sites due to the preloading is an active and significant mechanism, and
- the load-cool-fracture (LCF) load path is more beneficial than the load-unload-cool-fracture (LUCF). Hence, the change of yield strength mechanism is found to be the most beneficial mechanism.

Relevance

SSM intend to consider the results from all three projects when revising the section on WPS in SSM 2018:20 and as such use it as a scientific base for guidance and regulatory review.

Need for further research

This is the first of three projects researching WPS that SSM have planned. This first project investigated the mechanisms that contribute to the WPS effect, both numerically and experimentally.

The next project will develop a non-local probabilistic model for cleavage fracture that accounts for effects of load history and changes in temperature. This project will also investigate the effect of load history on brittle fracture.

The third project shall experimentally evaluate the margins to fracture associated with WPS. The analytical model developed in the previous project shall also be validated.

Since defects are usually found in welds, the interaction between weld residual stresses and WPS should be investigated. This is, however, outside the scope of the above mentioned three projects.

Project information

Contact person SSM: Daniel Kjellin
Reference: SSM2015-3853 / 2070004-34

Strål
säkerhets
myndigheten
Swedish Radiation Safety Authority

Authors: Tobias Bolinder[1], Alexander Eriksson[1], Jonas Faleskog[2],
Irene Linares Arregui[2], Martin Öberg[2], Bård Nyhus[3]

[1]Kiwa Technical Consulting AB, Stockholm, Sweden
[2]Royal Institute of Technology, Department of Solid Mechanics, Stockholm, Sweden
[3]SINTEF, Trondheim, Norway

2022:04

Warm Pre-Stressing mechanisms

Date: March 2022
Report number: 2022:04
ISSN: 2000-0456
Available at www.stralsakerhetsmyndigheten.se

This report concerns a study which has been conducted for the Swedish Radiation Safety Authority, SSM. The conclusions and viewpoints presented in the report are those of the author/authors and do not necessarily coincide with those of the SSM.

SSM 2022:04

Summary

The embrittlement of the reactor pressure vessel (RPV) due to extended operation can lead to difficulties in demonstrating safe operation beyond 40 years. But by utilizing the warm pre-stressing (WPS) effect in assessments, safe operation for continued operation beyond 40 years of the RPV may be shown. The WPS effect is the increase of the apparent brittle fracture toughness for a ferritic component when pre-loaded in the ductile upper shelf region and then cooled to the brittle lower shelf region of the material fracture toughness transition curve. The practice of utilizing the beneficial WPS effect in RPV assessments have been adopted in USA, Russia and some European countries.

Within this research project the four main mechanisms behind the WPS effect and their importance relating to RPV assessments were evaluated using both numerical methods and experiments. This research project answered the question of which of these four mechanisms, or combination of the four, is the governing mechanism in situations that can arise in a RPV.

The numerical work showed that for a realistic load case the most influenceable mechanism behind the WPS effect is the change in yield strength due to lowering of the temperature.

The experimental work showed that for a realistic load case the deactivation of initiation sites is also an active mechanism.

Furthermore, the actual load path can be considered path independent during the unloading/cooling phase assuming that the load is not increased during cooling.

Sammanfattning

Bestrålningsförsprödning av reaktortanken vid långtidsdrift kan i vissa fall leda till problem med att visa på en fortsatt säker drift över 40 år. Genom att tillgodoräkna sig varm förbelastning eller ”warm pre-stressing” (WPS) i utvärderingen av reaktortanken finns en möjlighet att visa på tillräckliga marginaler för fortsatt säker drift över 40 år. WPS effekten är den synbara höjningen av materialets brottseghet i klyvbrottsområdet som kan observeras i fall där komponenten förbelastas i det duktila området och sedan kyls till klyvbrottsområdet där det sedan belastas till brott. WPS effekten har tillämpats i säkerhetsutvärderingar av reaktortanken i bl.a. USA, Ryssland och några europeiska länder.

Syftet med detta forskningsprojekt var att studera de fyra huvudmekanismerna bakom WPS och deras betydelse vid utvärdering av reaktortanken. Mekanismerna studerades både med hjälp av numeriska metoder samt experimentellt. Projektet besvarade vilken av de fyra huvudmekanismerna, eller kombination av dessa, som är dominerande i situationer som kan uppstå för en reaktortank.

De numeriska analyserna visade att för en realistisk lasthändelse hos reaktortanken är den dominerande mekanismen bakom WPS förändringen av sträckgränsen på grund utav sänkt temperatur.

De experimentella resultaten kunde visa att för en realistisk lasthändelse hos reaktortanken är även utslagning av initieringspunkter en aktiv mekanism bakom WPS.

Vidare så konstaterades att den faktiska lastvägen kan ses som vägoberoende under kylningen hos lasthändelsen så länge som lasten inte ökar under kylning.

Table of Content ***Page***

1. Introduction

Brittle fracture is a disastrous event that can occur to ferritic steels at lower temperatures. In this temperature range the steel experience a significantly lower fracture toughness and the fracture is typically associated with sudden structural collapse. This region is called the (brittle) lower shelf region of the material fracture toughness curve. In Figure 1.1 a typical material fracture toughness curve of a ferritic material is illustrated.

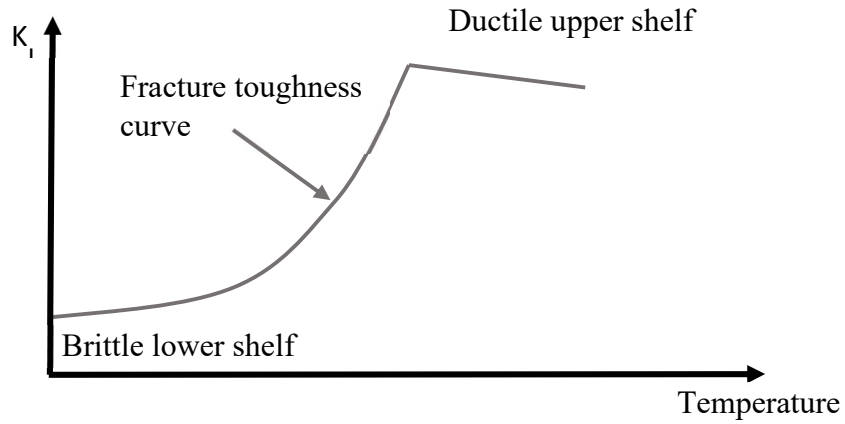

Figure 1.1. Material fracture toughness curve of a typical ferritic steel.

The problem is usually avoided entirely by ensuring that the component is operated in a temperature range where the steel is ductile. This temperature range is also known as the (ductile) upper shelf region. This is, however, not always possible. One such example is when considering long time operation (LTO) of the reactor pressure vessel (RPV) in a nuclear power plant. Irradiation induced embrittlement of the RPV shifts the temperature range for the ductile region of the steel in such a way that certain loading conditions can lead to difficulties in demonstrating safe operation when using traditional assessment methods. But by utilizing the beneficial warm pre-stressing (WPS) effect in assessments, safe continued operation of the RPV may still be shown.

The WPS effect is the increase of the apparent brittle fracture toughness for a ferritic component when pre-loaded at a temperature in the upper shelf region and then cooled to the lower shelf region of the material fracture toughness transition curve. The practice of utilizing the beneficial WPS effect in RPV assessments have been adopted in USA, Russia and some European countries.

There is a need to thoroughly evaluate the importance of the main mechanisms behind WPS in situations that could be encountered in a RPV in order to understand the limitations and possibilities in the engineering methods used to assess the WPS effect.

The mechanisms related to the introduction of a beneficial compressive residual stress field in front of the crack tip and the change of material properties due to lowering of temperature is studied with numerical methods. This is done using FE-analyses. To be able to quantify the contribution to the WPS effect from each mechanism a post processor utilizing a modified version of the non-local probabilistic model made by Kroon and Faleskog [1] is used for calculating the fracture probability.

The mechanisms related to deactivation of cleavage initiation sites and the blunting of the crack tip is studied with an experimental program. The purpose with the experimental program is to isolate the different effects from these four mechanisms to be able to evaluate their importance. Within the experimental program a fractographical examination of a large number of specimens is also done to identify the initiation sites for the brittle fracture.

The work described in this report answers which of the main mechanisms that are active and contribute to the WPS effect for situations that can arise in a RPV. This leads to an understanding of the possibilities and limitations of the engineering methods for WPS. Hence, the report clarifies the limitations for safe use of engineering methods for utilizing the WPS effect in RPV integrity assessments.

2. Theoretical background

2.1. Cleavage Fracture

Cleavage fracture is when a microcrack, generated by an imperfection in the material and subjected to a load, propagates through the material and causes structural collapse. What characterizes cleavage fracture is that the crack propagates by transgranular fracture in an unstable manner. This means that once the microcrack starts to grow it will not stop growing. This unstable crack growth means that the crack will rapidly tear through the material and cause sudden structural collapse.

Microcracks are initiated by imperfections in the material which cause high local stresses. Inclusions are small nonmetallic particles, imperfections, embedded in the material, see Figure 2.1, and have different material properties compared to the matrix material. This difference causes high local stress fields around the inclusions which can initiate cleavage fracture. One example of inclusions are carbides, which is carbon that has bonded to other metals. For cracked geometries the positions of initiation points in the material is one of the governing factors that determines the external load required to achieve cleavage fracture, this will be discussed in more detail later in this chapter. However, since the positions of these initiation sites are unknown prior to fracture, it is impossible to deterministically predict the fracture toughness of a material in the lower shelf region. Cleavage fracture is thus always associated with probabilistic approaches.

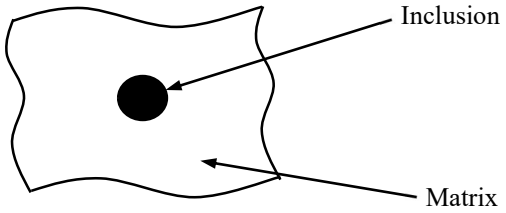

Figure 2.1. An inclusion located in an infinitesimal volume element of a ferritic matrix material.

The remainder of Chapter 2.1 will describe cleavage fracture on a close-to-micromechanical level and break the event down into three parts, namely the breaking of an inclusion, initiation of a microcrack and propagation into the matrix material.

2.1.1. Breaking of Inclusions

During loading, the inclusions tend to break before the matrix material. McMahon and Cohen [2] made several experiments on flat tensile specimens. They looked at the tendency of carbides acting as initiation

points for microcracks on two different steels at varying temperatures. At higher temperatures, more carbides tend to break without causing structural collapse. At lower temperature, however, the few carbides that do break have a higher tendency to cause structural collapse. They thus assumed that inclusions always break before the matrix material. Furthermore, it should be noted that the exact criterion for an inclusion to break is unknown but from McMahon and Cohen's article it appears to be a strain driven event. Stec [3] has made a micromechanical model which evaluates the stresses in the inclusion depending on material differences but also the shape and orientation of the inclusion. The shape and orientation of inclusions introduce another uncertainty which also contributes to scatter in the fracture toughness for cleavage fracture. However, in this report the problem is simplified by assuming that all inclusions are spherically shaped and thus have no specific orientation.

2.1.2. Initiating a Microcrack

When an inclusion breaks one of two things can occur. Firstly, the inclusion can separate from the matrix and create a small spherical void. If the inclusion separates from the matrix material, then no sharp edge will be created and the spherical void will then primarily expand due to further plastic straining at a rate governed by stress triaxiality. It can therefore not initiate a microcrack and can thus not cause cleavage fracture.

Secondly, if the inclusion breaks but does not separate from the matrix it can be seen as a Griffith flaw in the matrix material, see Figure 2.2. This would mean that the critical stress σ_f needed in the matrix material to propagate a microcrack can be calculated, see Equation (2.1).

$$\boldsymbol{\sigma_f} = \sqrt{\frac{\boldsymbol{\pi E \gamma_s}}{\boldsymbol{2(1-\nu^2)a}}} \tag{2.1}$$

Equation (2.1) is the Griffith equation for a penny-shaped crack where E is the young's modulus, γ_s is the surface energy of the material, ν is the poisson's ratio and a is the radius of the penny-shaped crack which in this case is the radius of the inclusion. The Griffith flaw is explained thoroughly in T.L. Andersson's book Fracture Mechanics, Fundamentals and Applications, Second Edition, pages 31-38 [4].

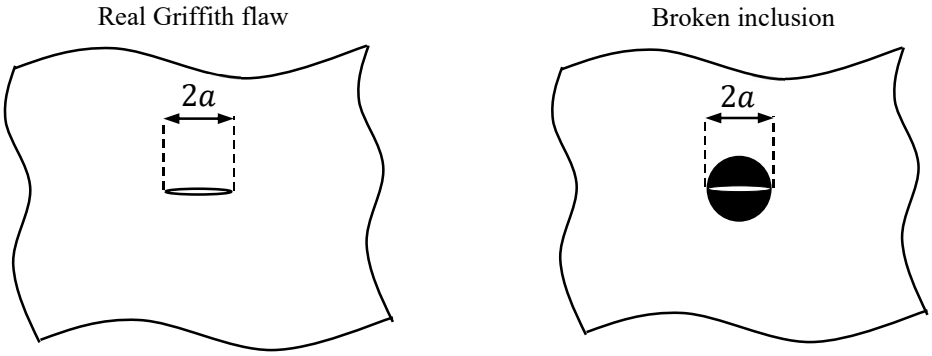

Figure 2.2. A Griffith flaw to the left and a broken inclusion to the right. From the Figure the similarities and differences between a real Griffith flaw and a broken inclusion can be seen.

It should be noted that a broken inclusion is not a perfect Griffith flaw. The Griffith flaw criterion is meant to evaluate the critical stress for a crack to propagate in the matrix, not the critical stress for a microcrack to be generated in the matrix. Furthermore, due to the difference in material properties a different stress field, from the one assumed by the Griffith flaw, is obtained. However, the inclusion is broken in such a way that it will not significantly affect the opening stress of the Griffith flaw. Thus, the assumption that the cracked inclusion can be seen as a Griffith flaw is motivated. For further discussion, see Kroon and Faleskog [5]

If the stress in the matrix material is equal to or greater than σ_f in Equation (2.1) then the broken inclusion will nucleate a microcrack that propagates into the matrix material. Inclusions can be found inside grains or at grain boundaries. Figure 2.3 shows a broken inclusion which is embedded in a grain. The microcrack propagates straight into the grain, in which it is embedded, and will keep a straight propagation plane until the grain boundary is reached.

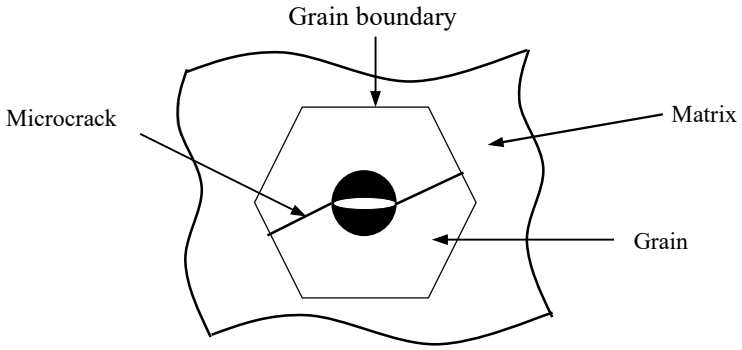

Figure 2.3. An illustration of a broken inclusion which has created a microcrack in the matrix material.

2.1.3. Propagation of the Microcrack

Once a microcrack has nucleated it will propagate through the material until it reaches a free surface, such as the macroscopic crack, or arrest.

The microcrack propagates in the plane that requires the least amount of energy to break. This plane is called the primary cleavage plane. The primary cleavage plane in each grain is different since the orientation of atomic structure in each grain differs. Furthermore, the primary plane of a neighbouring grain can be tilted in such a way that secondary cleavage planes are needed to connect the primary cleavage planes, see Figure 2.4.

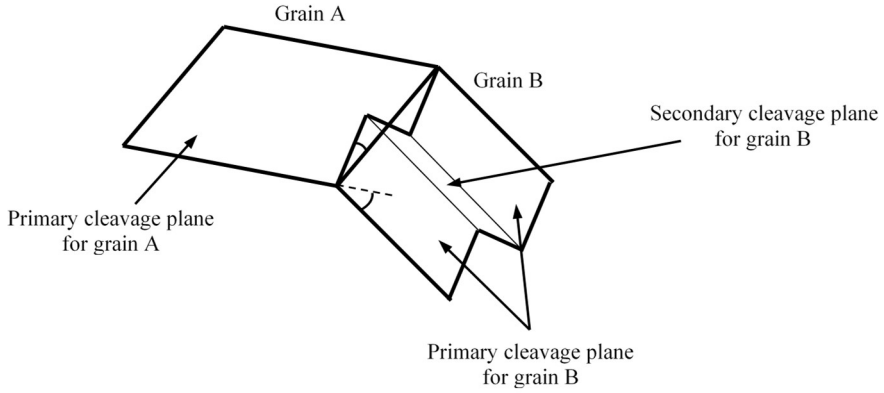

Figure 2.4. An illustration of how a microcrack propagates from grain A into grain B which changes the plane of propagation.

This means the microcrack will change its propagation plane when it reaches a grain wall which forms the so-called river patterns. It is possible to follow these river patterns back to the inclusion which served as an initiation point of the cleavage fracture. It is, however, known that the microcrack can arrest instead of causing structural collapse. From experiments made by McMahon and Cohen [2] it can be seen that it can arrest inside a grain due to twinning and also at grain boundaries which Lin et al. [6] has shown in experiments.

If the sharp tip of a growing microcrack is arrested, it will deform plastically and the sharp edge will be blunted, removing the stress singularity and severely lowering the stress at the edge of the microcrack. If the load is increased after the microcrack has arrested, the blunted microcrack will become a spherical void. Such a void cannot cause cleavage fracture due to this blunting.

It is hard to determine when the microcrack will propagate through a grain wall and when it will arrest. Ritchie et al. [7] suggested that a length scale should be used. They proposed that, instead of only satisfying Equation (2.1), the stress need to be above a certain threshold over a certain distance from the inclusion in order to cause structural collapse. In their article it is suggested that this distance should be related to the microstructure of the material and that its magnitude

should be in the order of grain diameters. Their theory was, however, disproven with tests made by Bowen et al. [8]. They conclude that the size of the 'process zone' should increase with temperature which means that the length scale should depend on temperature instead of being fixed to a microstructural entity. Furthermore, Kroon and Faleskog [5] later introduced viscoplastic effects into their model, introducing temperature dependent parameters. In the present report the Kroon's and Faleskog's model described in [1] will be used in which the length scale is assumed to be independent of temperature but generally obtains a value greater than the size suggested by Ritche et al. [7].

In Figure 2.5 the simplified event of cleavage fracture, as explained above, is summarized and illustrated as a flow chart.

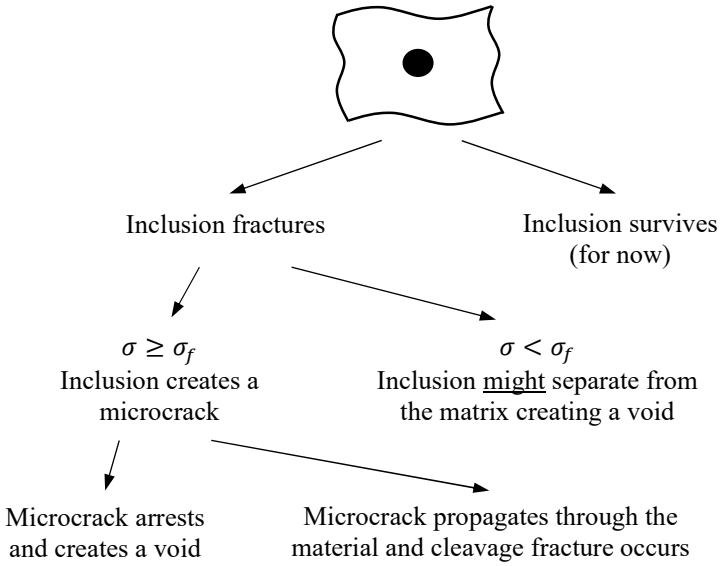

Figure 2.5. The event of cleavage fracture simplified and described in the form of a flow chart.

2.1.4. The Probabilistic Part of Brittle Fracture

The position of the inclusions in the material matrix influences the tendency for cleavage fracture. This can be understood by the fact that the position of the peak stress is dependent on the load. This is illustrated in Figure 2.6, showing the normal stress ahead of a crack at a certain load level. As the load increases, the peak will move further away from the crack tip and the stress profile will become wider. Given that the inclusion has enough energy to propagate a microcrack into the macroscopic crack, only a certain region in the material can fulfil the critical stress in Equation (2.1). From Figure 2.6 it can be seen that inclusion a will fulfil Equation (2.1) before inclusion b. But if there is no inclusion a then the external load can be increased until inclusion b

causes cleavage fracture. Hence, the critical load level for cleavage fracture is highly dependent on the position of the inclusions and the event of cleavage fracture is associated with significant scatter in the fracture toughness.

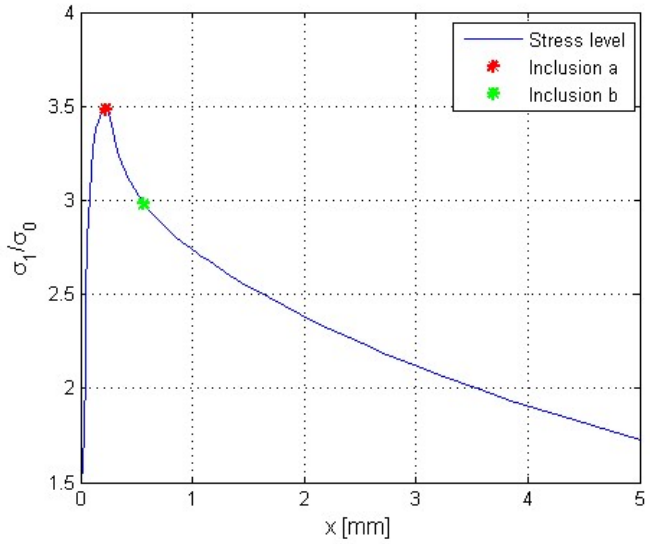

Figure 2.6. The stress in front of a blunted macroscopic crack tip plotted against the distance from the crack tip. The stars indicate the position of inclusions.

An interesting note to make here is that the number of inclusions, near the macroscopic crack, in a specimen also determines the fracture toughness. This means that cleavage fracture is dependent on the geometry of the crack front. An example of this is the width of a SEN(B) specimen. The probability that an inclusion is positioned close to the crack front is increased if the width of the crack front is increased. Thus, a wide crack front will predict a lower expected fracture toughness than a thin crack front.

As mentioned in Chapter 2.1.1 the shape and orientation of inclusions introduces another probabilistic event into cleavage fracture. It is shown in Stec's [3] micromechanical model that the shape and orientation can greatly affect the stress within the inclusion and thus also the external load required to fracture the inclusion. This is, however, as previously mentioned neglected in this report since all inclusions are assumed to have a spherical shape.

2.2. Warm pre-stressing (WPS)

To explain the WPS effect let us consider a structure with a crack like defect. The structure is loaded in tension at a temperature corresponding to the ductile upper shelf region of the material and unloaded either completely or partially. The structure is then cooled to the brittle lower shelf region of the material fracture toughness transition curve and, when reloaded, fracture occurs at a higher load than what is expected. This phenomenon of an apparent increase in the brittle fracture toughness of a ferritic component when pre-loaded at a temperature in the ductile upper shelf region is called the warm pre-stressing effect (WPS effect).

In Figure 2.7, the LUCF (Load Unload Cool Fracture), LCF (Load Cool Fracture) and CF (Cool Fracture) load paths, are illustrated. These load paths are frequently used in experiments to demonstrate the WPS effect. LUCF and LCF represent two extremes and a realistic load path is something in between these two. An example of a realistic load path is shown in Figure 2.8 which shows a simulation of an elliptic surface crack in a RPV subjected to a LOCA (Loss of Coolant Accident) load case.

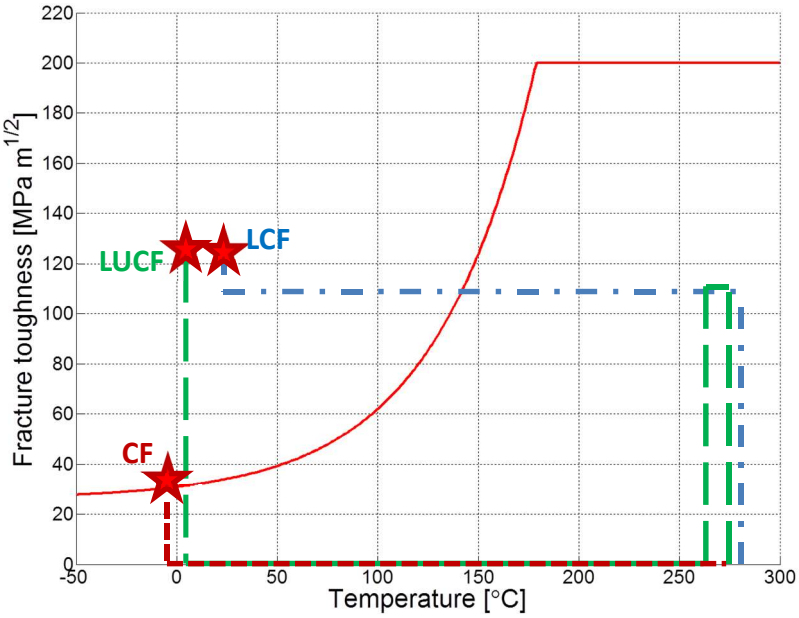

Figure 2.7. Cool Fracture, Load Cool Fracture and Load Unload Cool Fracture load paths illustrated together with a material fracture toughness curve (red line).

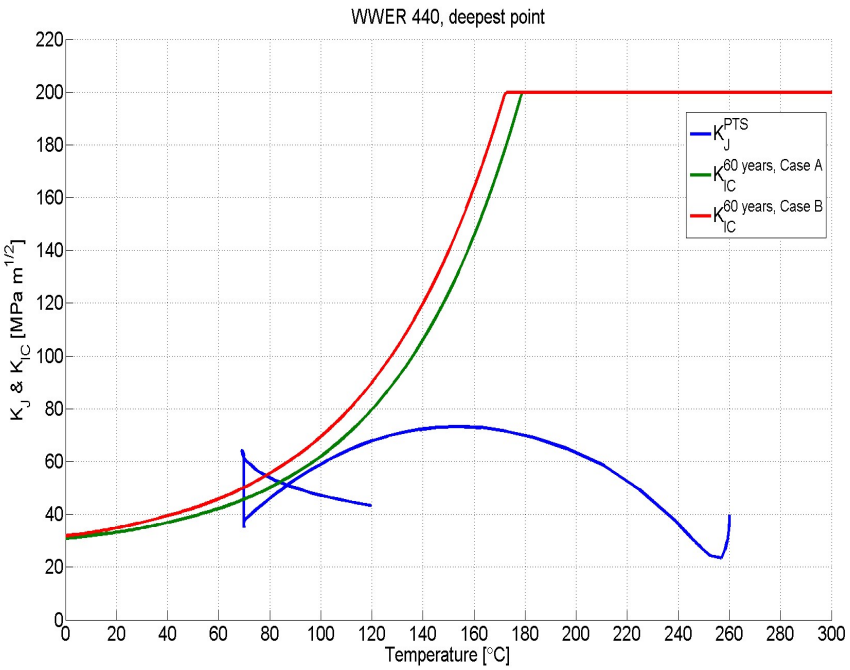

Figure 2.8. Example of realistic load path, blue line, for a elliptic surface crack in a RPV subjected to a LOCA load case.

The existence of the WPS effect is thoroughly established. Several published works have earlier shown the existence of the WPS effect. Experiments have been done by Smith et al. [9] and Yuritzinn et al. [10] where they confirmed the WPS effect by doing several LUCF load cycles. Chapuliot et al. [11] performed several tests on as-received, thermal treated and irradiated VVER 440 reactor pressure vessel steel. They looked at several different load paths LUCF, LCF, Load-Partial-Unload-Cool-Fracture (LPUCF), Load-Partial-Transient-Unload-Fracture (LPTUF) and Load-Transient-Unload-Fracture (LTUF). Large scale test showing the WPS effect have also been performed by Moinereau et al. [12].

The WPS effect is, in this report, attributed to four main mechanisms.

- Introduction of a beneficial compressive residual stress field in front of the crack tip, due to local plastic deformation from the preloading and unloading
- Change of yield properties due to lowering of temperature
- Deactivation of cleavage initiation sites by pre-straining
- Blunting of the crack tip

These mechanisms can be expected to have different impact, depending on the load path and pre-load level. All the mechanisms are related to plastic straining at pre-load. The remainder of Chapter 2.2 will explain the four mechanisms in more detail.

2.2.1. Introduction of beneficial compressive residual stress field

During the WPS load transient the unloading of the structure will result in a compressive residual stress field around the macroscopic crack tip due to the plastic deformation created during the pre-loading. After unloading the structure, the material will attempt to return to its undeformed state. This causes the surrounding material to compress the highly plastically deformed region near the macroscopic crack tip, resulting in a compressive residual stress field. This compressive residual stress field remains as the temperature is lowered. When the specimen is reloaded in the brittle lower-shelf region the compressive residual stress field will reduce the opening stress around the macroscopic crack tip. By lowering the opening stress near the crack tip, the volume in which the stresses are high enough to fulfil Equation (2.1) is reduced and thus the probability of cleavage fracture is also reduced. Figure 2.9 illustrates how the residual stress field affects the opening stress in front of the macroscopic crack tip.

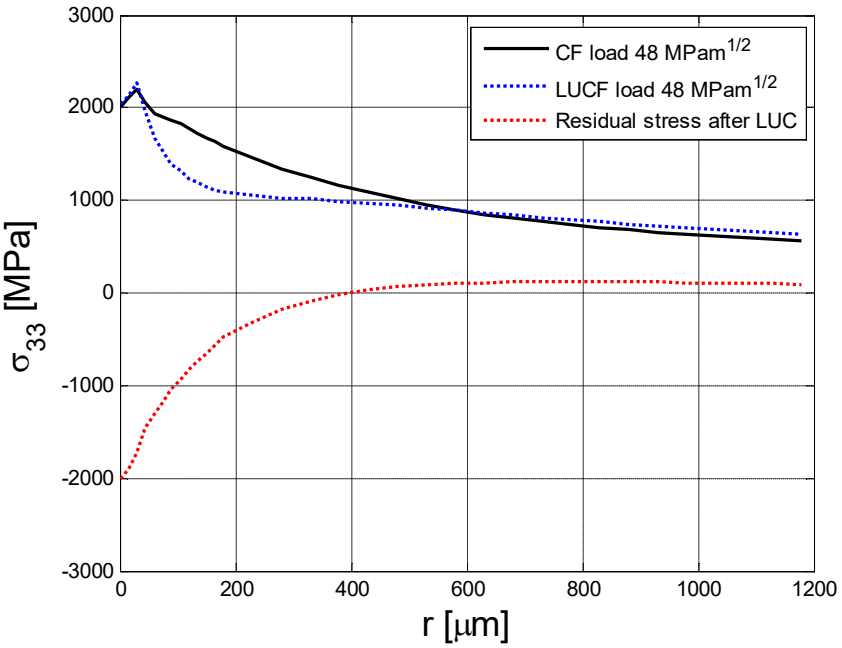

Figure 2.9. Opening stress in front of the macroscopic crack tip for a cool fracture cycle and a Load-Unload-Cool-Fracture (LUCF) load cycle after cooling and reloading.

When reloading the specimen in the brittle lower-shelf region, the material will deform plastically at the crack tip of the macroscopic crack. The active plastic zone will therefore start at the crack tip and then grow as the load is increased. This yields a high stress gradient at the border of the active plastic zone. This means that a volume which experiences a low stress due to the residual stress field can quickly

change into a high stress state when entering the active plastic zone. Thus, a wider spread in experimental data, compared to the cool fracture load cycle, is expected.

2.2.2. Change of yield properties due to lowering of temperature

The yield surface of a material increases as the temperature decreases and vice versa. This means that a structure loaded in the ductile region will experience more plastic strains than if it was loaded in the brittle region with the same external force.

Now assume that the structure, loaded in the ductile upper-shelf region, is moved to the brittle lower-shelf region by changing the temperature in such a way that the stress field is unchanged. By lowering the temperature, the yield strength will increase and the yield surface will expand. Hence, the elastic and plastic strains will not change and therefore the stress field also remains unchanged. This means that the specimen loaded in the ductile region and then moved to the brittle region will experience a lower stress field than the specimen directly loaded in the brittle region even if the specimens are exposed to the same external load. This is illustrated below in Figure 2.10.

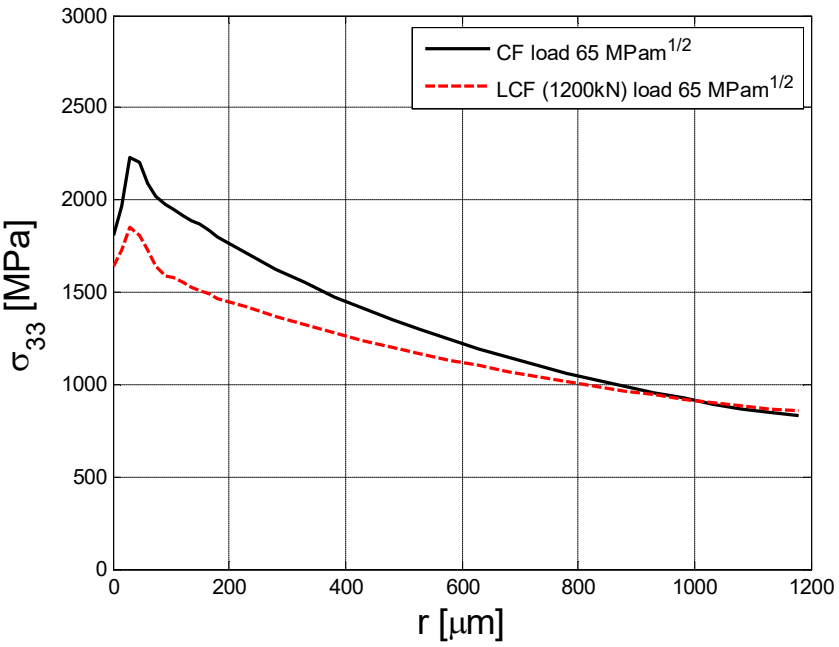

Figure 2.10. Opening stress in front of the macroscopic crack tip for a CF load cycle and a LCF load cycle.

From Chapter 2.1 it can be deduced that cleavage fracture can only occur if the load at an initiation point is increased. This, however,

appears to be a very unstable event. Chapuliot et al. [11] have recorded specimens failing due to cleavage fracture during the cooling phase of the LCF load cycle. This suggests that the margins to fracture during the cooling phase are small. Hence, a small increase in load during the cooling phase could cause cleavage fracture.

2.2.3. Deactivation of cleavage initiation sites

During the WPS cycle, when the structure is pre-loaded in the ductile upper-shelf region, inclusions near the crack tip can separate from the matrix material and/or break due to high strains near the crack tip. The inclusions that separate and/or break during this pre-load do not lead to fracture of the structure. For example, if the inclusions separate from the matrix material a void is created, which cannot cause cleavage fracture. If the inclusion does not separate and instead break and creates a microcrack in the matrix material then the microcrack will arrest at nearby grain walls, due to the high temperature causing increased plastic dissipation. As stated before, an arrested microcrack will quickly blunt and generate a void in the material. Hence, all inclusions that fractured in the ductile region during the pre-load are inactive in the cleavage fracture event. These inclusions are deactivated.

2.2.4. Blunting of the cracktip

Since the pre-loading is done in the ductile region cleavage fracture cannot occur and a higher load can be applied without experiencing structural collapse. This gives a large plastic region and high plastic strains around the crack tip. The plastic strains will blunt the sharp crack tip and the theoretic stress singularity will be lost. The stress field around the vicinity of the crack tip will therefore be reduced which makes the region, in which the stress is high enough to cause cleavage fracture, smaller thus reducing the probability of cleavage fracture.

3. Numerical work

As mentioned in the introduction, the mechanisms of the WPS effect related to the introduction of a beneficial compressive residual stress field in front of the crack tip and the change of material properties due to the lowering of temperature is studied with numerical methods. This is done using FE-analyses. In order to compare the two mechanisms a post-processor was created for computing the probability of cleavage fracture. The model used in order to calculate the probability of cleavage is a modified version of the model proposed by Kroon and Faleskog [1]. The model will be further explained below.

3.1. Probabilistic model of brittle fracture

The weakest link model is typically used in order to calculate the probability of cleavage fracture. The idea is that the specimen is divided into infinite amounts of infinitesimal volume elements and each element has a certain risk of failing. It is assumed that if one element fails the entire specimen experiences structural collapse and that the probability of failure for each element is independent of other elements.

It is assumed that the probability of an infinitesimal element failing only depends on the load applied to the element and the volume of the element. In this way the probability that an inclusion exists in the infinitesimal element volume does not need to be considered.

A weakest link model commonly used is the two parameter Weibull model shown in Equation (3.1).

$$P_f = 1 - exp\left(-\frac{B}{B_0}\left[\frac{K_I}{K_0}\right]^4\right) \tag{3.1}$$

However, the two parameter Weibull model have a few weaknesses. First of this model has no lower bound which means that for any load level, no matter how small, there is a finite probability for cleavage fracture. Secondly the model tends to over predict the amount of experimental scatter [13]. These weaknesses can be corrected by incorporating a third parameter, K_{min}, see Equation (3.2).

$$P_f = 1 - exp\left(-\frac{B}{B_0}\left[\frac{K_I - K_{min}}{K_0 - K_{min}}\right]^4\right) \tag{3.2}$$

This model is called the three parameter Weibull model. With the third parameter it is possible to create a lower bound as well as lowering the standard deviation.

Other probabilistic models exist. For example, Lefevre et al. [14] proposed two probabilistic models. One that evaluated the probability of cleavage from stresses within the plastic zone and another which used the same formulation but only evaluated stresses from the active plastic zone, $d\varepsilon^p > 0$. Both were modifications of the Beremin model [15].

3.2. The non-local probabilistic model

In the model proposed by Kroon and Faleskog [1] the failure probability of the infinitesimal volume element, dP_f, depends on a non-local measurement of the maximum principal stress, the equivalent plastic strain and the volume of the element, see Equation (3.3).

$$dP_f = h\left(\varepsilon_e^p, \bar{\sigma}_1\right)\frac{dV}{V_0} \tag{3.3}$$

V_0 in Equation (3.3) is a constant put into the equation in order to make the dimension of dP_f correct. V_0 is chosen arbitrarily and the reason for this will be explained later in this section. The function h in Equation (3.3) is separated into a product of two functions, $h_1(\varepsilon_e^p)$ and $h_2(\bar{\sigma}_1)$. The idea is to separate the tendency of fracturing inclusions and the risk of a fractured inclusion leading to cleavage fracture. The function h_1 is meant to describe the probability of inclusions fracturing. From experiments made by Gurland [16] it can be seen that the number of cracked carbide particles seem to be proportional to strain. McMahon and Cohen [2] showed similar results but discovered that this trend only applies below a certain temperature. Therefore, it is assumed in the probabilistic model made by Kroon and Faleskog [1] that the probability of an inclusion breaking is proportional to plastic strain. The h_1 function is shown in Equation (3.4).

$$h_1\left(\varepsilon_e^p\right) = c\varepsilon_e^p \tag{3.4}$$

The parameter c in Equation (3.4) is meant to quantify the effect that plastic strain has on the fracturing of inclusions and how many of these inclusions that could eventually lead to cleavage fracture. Note that the function h_1 is not a probabilistic function and can thus only be seen as an indication that more inclusions break if the equivalent plastic strain is increased.

There are certain complications when using Equation (3.4). For example when evaluating the probability of failure on a specimen with a prior plastic deformation, the h_1 function will yield a high value even if no external load is applied to the specimen due to the high equivalent plastic strains. Thus the h_1 function must be modified in order accurately describe the number of possible initiation points even if the

effects of a load history are present. Therefore, out of necessity a modified version of h_1 is being used in this work, see Equation (3.5).

$$h_1\left(\varepsilon_e^p\right) = c\left(\varepsilon_e^p - \varepsilon_{e0}^p\right) \tag{3.5}$$

In Equation (3.5) the variable ε_{e0}^p is the accumulated equivalent plastic strain at the start of reloading and ε_e^p is the current equivalent plastic strain. This means that all equivalent plastic strain accumulated up to the point of reloading will be considered harmless.

The function h_2 handles the local stress criterion for initiation of a microcrack as well as the non-local stress criterion for the microcrack to propagate further. The size of the inclusions in the material is assumed to follow an exponential distribution as the one seen in Equation (3.6).

$$p(l) = \frac{1}{\alpha} exp\left(-\frac{l}{\alpha}\right) \tag{3.6}$$

In Equation (3.6) α is the mean value of the exponential distribution and l is the characteristic size of a possible inclusion. Assuming that the largest possible inclusion which can lead to cleavage fracture has the characteristic length l_{th} it is possible to calculate the corresponding threshold stress, σ_{th}, for that inclusion with Equation (2.1). Let an infinitesimal element volume be exposed to the non-local stress measure $\bar{\sigma}_1$ such that $\bar{\sigma}_1 > \sigma_{th}$. The smallest broken inclusion which would initiate a microcrack at this stress level could then be calculated with Equation (2.1), let this inclusion have the characteristic size l_1. This means that any broken inclusion with a characteristic size l, such that $l_1 \leq l \leq l_{th}$, will initiate a microcrack in the material. The probability that the infinitesimal element volume contains an inclusion of such size can be derived from Equation (3.7). The h_2 function is equal to this probability.

In order to calculate the h_2 function, the probability $p(l_1 \leq l \leq l_{th})$, Equation (3.6) has to be integrated from l_1 to l_{th}, see Equation (3.7).

$$\int_{l_1}^{l_{th}} \frac{1}{\alpha} exp\left(-\frac{l}{\alpha}\right) dl = exp\left(-\frac{l_1}{\alpha}\right) - exp\left(-\frac{l_{th}}{\alpha}\right) \tag{3.7}$$

By introducing $\sigma_m = k/\sqrt{\alpha}$, $\bar{\sigma}_1 = k/\sqrt{l_1}$, and $\sigma_{th} = k/\sqrt{l_{th}}$, the right hand side of Equation (3.7) can be rewritten into Equation (3.8).

$$h_2(\bar{\sigma}_1) = exp\left(-\left(\frac{\sigma_m}{\bar{\sigma}_1}\right)^2\right) - exp\left(-\left(\frac{\sigma_m}{\sigma_{th}}\right)^2\right), \quad \bar{\sigma}_1 \geq \sigma_{th} \tag{3.8}$$

The integral in Equation (3.7) and the use of Equation (2.1) is illustrated in Figure 3.1 below.

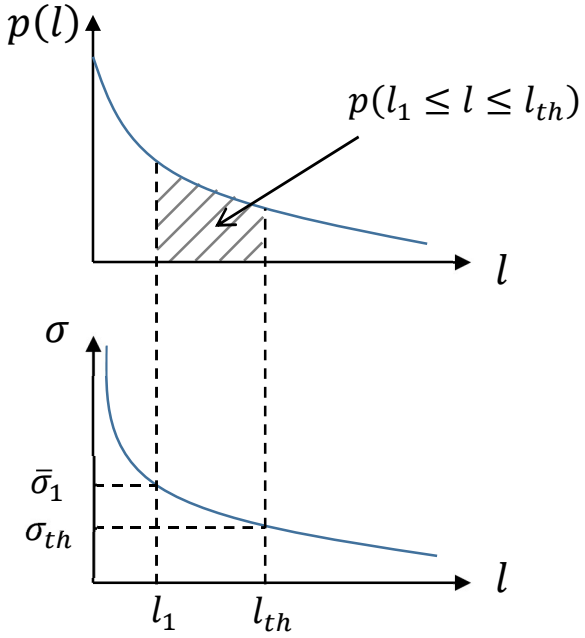

Figure 3.1. The exponential cumulative distribution of inclusion sizes and the Griffith flaw critical stress plotted against the characteristics size of the flaw. The shaded area shows the probability that an inclusion has a characteristic length between l_1 and l_{th}.

The choice of distribution in Equation (3.6) is motivated by observation of experimental data made by Lin et al. [6] as well as experiments made by Lee et al. [17]. It is assumed that this distribution is representative for most kinds of steels. It should be noted that in an exponential distribution, particles with infinitesimal size are most likely to be present. This is of course impossible since the particles must have a finite size. However, this is assumed to be negligible.

Moving on to the non-local stress measure, $\bar{\sigma}_1$, which is calculated with Equation (3.9). Instead of using the local stress, σ_1, an average of the local stress is made over the volume V_L. This way a non-local stress measure is obtained.

$$\bar{\sigma}_1 = \frac{1}{V_L}\int_{V_L} \sigma_1(\boldsymbol{x} - \hat{\boldsymbol{x}})\, dV, \quad |\boldsymbol{x} - \hat{\boldsymbol{x}}| \leq L \tag{3.9}$$

In Equation (3.9), the volume V_L can be chosen as a sphere or a cylinder depending on the shape of the crack front. For example, for a straight crack front the stress gradient along the thickness direction is relatively small compared to the stress gradient in the crack tip direction and crack normal direction. Thus, a cylindrical volume can be chosen when a straight crack front is modelled. For a penny-shape crack, however, a spherical volume should be chosen since the stress gradient varies in all three directions when using a Cartesian coordinate system. Note also

that the length parameter, L, can be set to zero in order to receive a local stress measure instead. The combination of the two parameters σ_{th} and L gives threshold value similar to K_{min} in Equation (3.2) and the model does therefore not predict cleavage at an infinitesimal load unless L or σ_{th} is chosen to be zero.

Now the probability that an infinitesimal element volume dV fails can be calculated by inserting Equation (3.4) and (3.8) into Equation (3.3). This procedure results in Equation (3.10).

$$dP_f = c\varepsilon_e^p \left[exp\left(-\left(\frac{\sigma_m}{\bar{\sigma}_1}\right)^2 \right) - exp\left(-\left(\frac{\sigma_m}{\sigma_{th}}\right)^2 \right) \right] \frac{dV}{V_0}, \quad \bar{\sigma}_1 \geq \sigma_{th} \quad (3.10)$$

In Equation (3.10), $\bar{\sigma}_1$ is calculated with Equation (3.9). The probability that the specimen will fail can now be calculated with the weakest link model. This results in Equation (3.11).

$$P_f = 1 - exp\left(-\sum_i dP_f^{(i)} \right) \quad (3.11)$$

It should be noted that the probability of any element failing, $dP_f^{(i)}$, should not decrease while the load is being increased. This can occur if the crack tip is blunted since the position of the stress peak then becomes load dependent. This means that even if the load is being increased certain elements can experience a reduction in principal stress and thus a decreased probability of failure. In order to prevent a decrease in $dP_f^{(i)}$ the maximum value from the start of the loading phase up to the current load is used in the calculation of P_f. Implementing this in equation (3.11) yields Equation (3.12) where j indicates the current load increment.

$$P_{f,j} = 1 - exp\left(-\sum_i \max\left(dP_{f,1}^{(i)}, dP_{f,2}^{(i)}, \dots, dP_{f,j}^{(i)} \right) \right) \quad (3.12)$$

The model contains four material parameters that must be calibrated, namely: c, σ_{th}, σ_m and L. However, Kroon and Faleskog show that Equation (3.11) has a weak dependence on σ_m for specimens containing a macroscopic crack. Therefore, a new material parameter, $\eta = \sigma_m/\sigma_{th}$, is introduced. Thus, by setting the ratio η to a fixed value, only three material parameters must be calibrated. In this work the value of η is set to 1 as Kroon et al. [18] did in their calibration of the model.

The major difference between the three parameter Weibull model and the one proposed in Equation (3.11) is that the three parameter Weibull evaluates the probability of failure exclusively on the value of K_I. This means that small scale yielding is assumed and that the constraint effect must be implemented as a tabular value. The model proposed by Kroon

and Faleskog calculates the probability of failure by evaluating the stress and strain field. This means that it can capture all changes in the stress and strain field such as constraint effects or a residual stress field. It is thus possible for this model to evaluate some of the WPS mechanisms which are not possible to evaluate with the Weibull model. The downside is that several finite element models must be created in order to calibrate and calculate the probability of failure.

3.2.1. The post-processor

A post-processing script was written in fortran. The purpose of the post-processing script was to generate a cumulative distribution function by evaluating Equation (3.12) with data generated by a finite element model. The first principal stress, equivalent plastic strain and coordinates were evaluated at the centroid of each element.

In order to discretize Equation (3.9) the distance between each element centroid was evaluated. Since the only straight crack fronts are being modelled; the volume V_L is formed as a cylinder. This means that the constraint in Equation (3.9) only applies in the x-y-plane, see Figure 3.2. Element j need to have the same undeformed z-coordinate as element i to be a part of the integral in Equation (3.9). The discretized version of Equation (3.9) is shown in Equation (3.13).

$$\bar{\sigma}_1(\boldsymbol{x_i}) = \frac{\sum_j^N \sigma_1(\boldsymbol{x_j})\Delta V^{(j)}}{\sum_j^N \Delta V^{(j)}}, \left\{ \begin{array}{c} \sqrt{\left(x_i - x_j\right)^2 + \left(y_i - y_j\right)^2} \leq L \\ z_i - z_j = 0 \end{array} \right\} \quad (3.13)$$

In Equation (3.13) $\Delta V^{(j)}$ is the undeformed volume of element j. x_j, y_j and z_j are the undeformed centroid coordinates for element j. N is the number of elements that fulfils the constraint.

It can be argued that the centroid coordinates should be taken from the deformed state in order to capture the increased elemental density at the crack tip. This effect was, however, assumed to be small and the extra elements entering the summation in Equation (3.13) will not change the value of $\bar{\sigma}_1$ noticeably. However, by using undeformed centroid coordinates, a lot of computational time can be saved since the constraint shown in Equation (3.13) only needs to be evaluated once.

The script also handled the parameter calibration as explained below in Chapter 3.2.2.

In order to find numerical probabilities of failure at load levels corresponding to the experimental load levels, see Equation (3.17), a piecewise linear function was created by linear interpolation between the load levels given by the finite element model.

3.2.2. Calibration of model

Two sets of experiments are needed in order to calibrate the model in such a way that it captures the constraint effect. One set of high constraint experiments, set A, and one set of low constraint experiments, set B. A cumulative distribution function needs to be created from the experimental data. This can be done by using an approximation suggested by Wallin [19] for median ranks shown in Equation (3.14) where i is the specimen number and N is the number of specimen in the experiment. Note that specimens are sorted from smallest to largest measured fracture toughness before evaluating Equation (3.14).

$$P_{fexp} = \frac{i-C}{N+1-2C} \tag{3.14}$$

The most accurate results are obtained by setting the variable C equal to 0.3 [19]. In the work presented within this report, however, the experimental data is fitted to a log-normal distribution. In order to evaluate a log-normal cumulative distribution function, the probability density function is integrated. The log-normal probability density function is shown in Equation (3.15).

$$p_{f,log-normal} = \frac{1}{x\sigma\sqrt{2\pi}} exp\left(-\frac{(\ln(x)-\mu)^2}{2\sigma^2}\right) \tag{3.15}$$

In Equation (3.15), μ is the mean value of the natural logarithm of the experimental data, σ is the standard deviation of the natural logarithm of the experimental data and x is the measured fracture toughness. In order to obtain the cumulative distribution function Equation (3.15) is either acquired by cumulatively integrating the log-normal probability density function or acquired by calculating the finite sum shown in Equation (3.16).

$$P_f(x) = 0.5 - \frac{1}{\sqrt{\pi}}\sum_{k=0}^{n}\frac{(-1)^k.\ \ 1+2k}{(1+2k)k!}, \quad \beta = \frac{\ln(x)-\mu}{\sqrt{2}\sigma} \tag{3.16}$$

In this project the cumulative distribution function is acquired through the finite sum shown in Equation (3.16).

In order to generate a good log-normal distribution to the experimental data; more experiments are typically needed than if Equation (3.14) is used. The log-normal distribution, however, yields a more realistic distribution since Equation (3.14) has the weakness that one critical load value is described with two different probabilities if two specimens fail at the same measured fracture toughness.

The parameters needed to calculate Equation (3.11), as well as the *J*-integral value, are extracted from a finite element model with the same

geometry and load case as the experimental specimens. The right hand side of Equation (3.11) is then compared with the experimental probability of failure calculated from Equation (3.16). In this work a least square method is used to compare the probabilities, as done by Kroon et al. [18], see Equation (3.17).

$$R_A = \sum_i^{N_A} \left(P_{fexpA}^{(i)} - P_f \right)^2 \Big|_{J=J_c^{(i)}},$$
$$R_B = \sum_i^{N_B} \left(P_{fexpB}^{(i)} - P_f \right)^2 \Big|_{J=J_c^{(i)}} \quad (3.17)$$

In Equation (3.17) N_A and N_B is the number of experiments done on the high constraint and the low constraint experimental sets respectively. $P_{fexpA}^{(i)}$ and $P_{fexpB}^{(i)}$ are the experimental probabilities of failure calculated from Equation (3.16) with x being the measured fracture toughness $J_c^{(i)}$. The index (i) indicates the specimen i out of a total of N_A or N_B specimens. The probability P_f is acquired from the finite element models by using the probabilistic model, see Equation (3.12). The total error, R_{LS}, is calculated as the sum of R_A and R_B.

The value of parameter c was calculated using the Golden Ratio for several combinations of L and σ_{th}. Note that the Golden Ratio is only guaranteed to find the global minimum if no local minimums exist. This is not quite the case here since the parameter c changes the standard deviation as well as the expected value of the cumulative distribution functions. Since the calibration is done on two sets of experiments at the same time it is possible for local minimums to appear since each set has its own optimal value of c. However, the local minima that might exist will be relatively close to the global minimum and the Golden Ratio is thus deemed to be good enough for the calibration.

It should also be noted that only the value of c is changed in the calibration and it is thus important that V_0 remains unchanged after the calibration. This also explains why the actual value of V_0 can be chosen arbitrarily and its only purpose is to give dP_f the right dimension. It should also be noted that the number of symmetry planes used in the finite element model must be taken into account since only a portion of the specimen's true volume is being simulated. In Equation (3.10) there should be an extra constant multiplied to the value of dP_f corresponding to the ratio between the specimen's true volume and the volume simulated in the finite element model. This is important if the volume fraction would change in another finite element model where for example only one symmetry plane is being used.

Appropriate intervals for L and σ_{th} are chosen and c is calculated using the Golden Ratio for each combination of L and σ_{th}. The combination that yields the smallest total error, R_{LS}, then represents the material parameters for the model.

3.3. Finite element model

3.3.1. Geometry and material

A total of four SEN(B) finite element models were created. Only a quarter of each specimen was modelled using symmetry boundary conditions. The geometry for the SEN(B) models is shown in Figure 3.2. In Table 3.1 the details of each SEN(B) model is shown. All models are modelled with hexahedral 8-node elements using full integration and a sharp crack with 8-node elements using collapsed uncoupled nodes at the crack tip. Cauchy stress, logarithmic strain and von Mises flow rule was used in all models. All load cases were modelled as quasi-static.

An example of the mesh used for the SEN(B) models is shown in Figure 3.3. Typically, around 40 000 – 50 000 elements were used in each model. Each model used in the calibration had 28 elements in thickness direction with a bias towards the free surface of the model. The model used to evaluate the WPS mechanisms had 56 elements in thickness direction without a bias.

It should be noted that the near crack tip meshes in the calibration models differs, see l_e in Table 3.1. The probabilistic model proposed by Kroon and Faleskog [1] is material dependent which means that it should be independent of the mesh around the crack tip if the mesh is fine enough to yield a good resolution of the stress field around the crack tip. This means that, as long as the stress field is correctly modelled, even if the mesh differs in between finite element models the probabilistic model will remain unaffected.

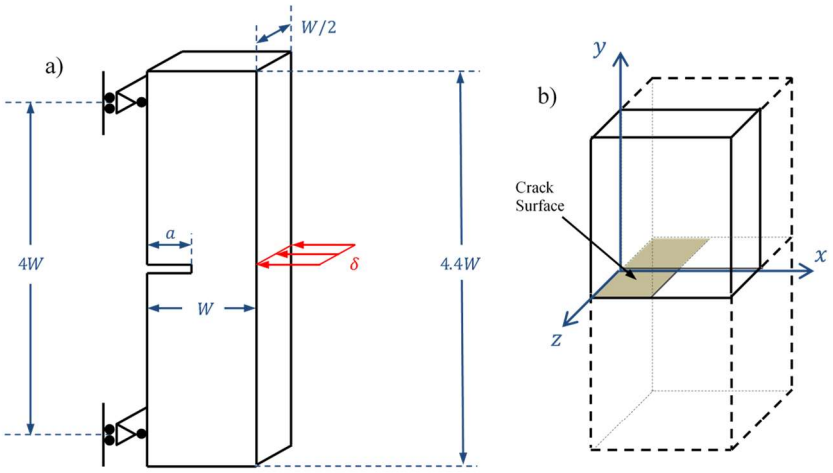

Figure 3.2. The parameterized SEN(B) geometry as well as the symmetry planes used in the Finite Element Analysis. In b) the box with full lines represents the actual FE model.

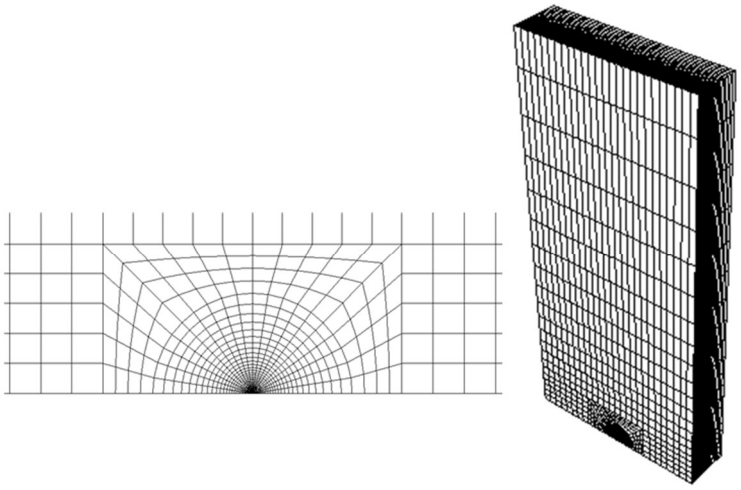

Figure 3.3. An example of the mesh used in the SEN(B) models.

Table 3.1. Geometry parameters for all SEN(B) finite element models. l_e is the length of the crack tip element.

Used for:	$W\ [mm]$	a/W	$l_e[\mu m]$
Calibration	40	0.50	21.0
Calibration	40	0.25	12.6
Calibration	40	0.10	3.9
Evaluation of WPS Mechanisms	40	0.50	11.5

The material used in all finite element simulations is equivalent to the material used by Kroon et al. [18] when they verified the probabilistic model. The material is defined by the Ramberg-Osgood material formulation shown in Equation (3.18).

$$\varepsilon = \frac{\sigma}{E} + \frac{\sigma_Y}{E}\alpha\left(\frac{\sigma}{\sigma_Y}\right)^n \tag{3.18}$$

Equation (3.18) was used to create an elastic multilinear plastic material model with isotropic hardening in order to capture load history effects on the material. The value of the parameters used in the material formulation is equivalent to the parameters acquired by Kroon et al. [18] and are shown in Table 3.2 and illustrated in Figure 3.4.

Table 3.2. Parameters used in the Ramberg-Osgood material formulation.

T[°C]	E $[GPa]$	v	σ_Y $[MPa]$	α	n
-30	208	0.3	597	0.62	8.5
25	208	0.3	557	0.56	9.4
55	208	0.3	552	0.50	10.0

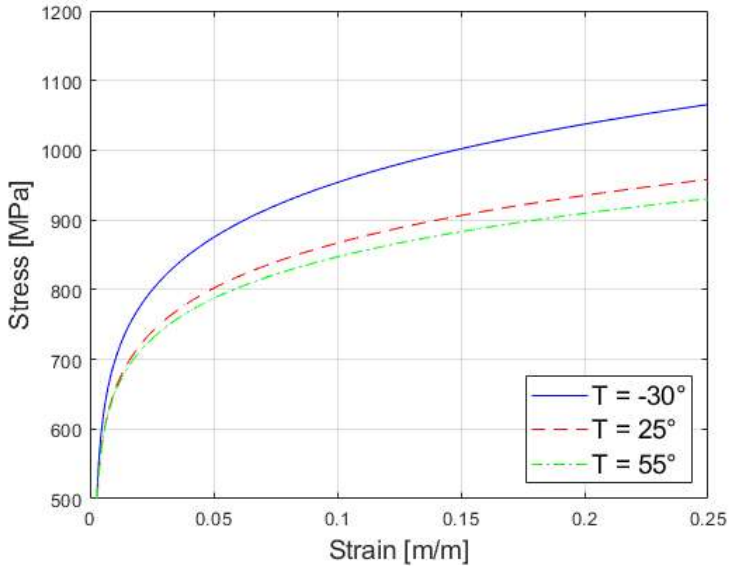

Figure 3.4. An illustration of the material curves described in Table 3.2.

3.3.2. Load and load cycles

The load was applied as the indentation δ in Figure 3.2. The indentation δ was applied by a rigid cylinder with radius $W/4$ which was pushed into the specimen. A state-based tracking algorithm for surface-to-surface contact with finite sliding was used with the rigid surface being the master surface and the side of the SEN(B) model acting as the slave surface. The tangential behaviour was set to frictionless. For more information about the algorithm see Contact formulations and numerical methods in Abaqus/Standard in the Abaqus documentation [20].

For the calibration, CF (isothermal) load cycles were used at a temperature of $-30°C$. The applied load in these load cycles were determined by the measured fracture toughness in the experiments.

An isothermal as well as three LCF and three LUCF load cycles were generated in order to measure the influence of each of the two mechanisms alone. The LCF and LUCF load cycles were done with three different pre-load levels at a temperature of $55°C$ before being reloaded at a temperature of $-30°C$. The load curves for LCF and LUCF can be seen in Figure 3.5 and Figure 3.6 respectively. The load

levels $J = 21\ kN/m$ and $J = 105\ kN/m$ shown in Figure 3.5 and Figure 3.6 corresponds to load levels A/B and C/D respectively in the RPV. These load levels are commonly measured in stress intensity factors but has in this work been recalculated to *J*-integral values using the small scale yielding assumption ($J = K_I^2/E'$). The highest load level, $175\ kN/m$, is an extreme load done in order to evaluate how the WPS effect scales. It should again be noted that the *J*-integral is not correctly evaluated when there is a residual stress field. Therefore, all load cycles which were used in evaluation of the WPS mechanisms has been plotted against the applied force divided by the limit load.

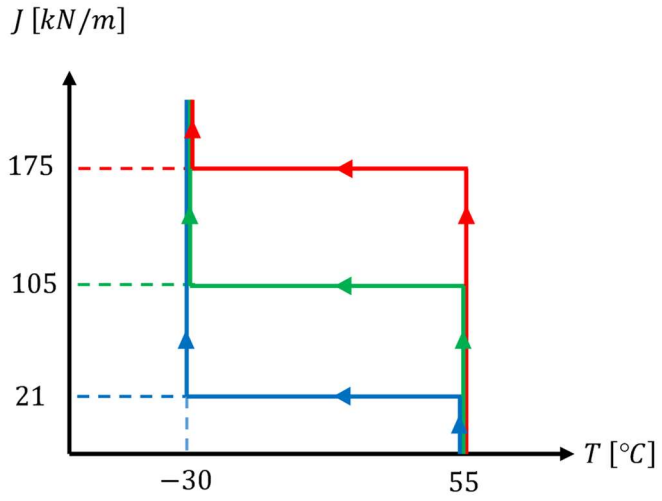

Figure 3.5. The Load-Cool-Fracture (LCF) load cycle with three different pre-loads.

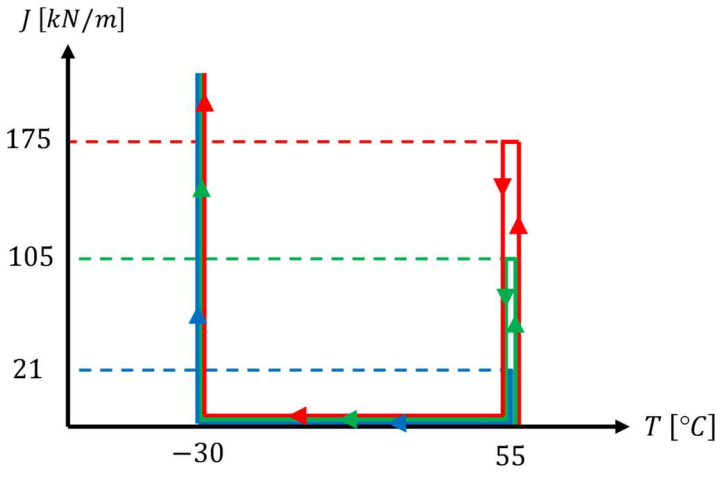

Figure 3.6. The Load-Unload-Cool-Fracture (LUCF) load cycle with three different pre-loads.

After the effect of each mechanism had been measured; more advanced load cycles were applied to the model. In order to see the effect of the load path, so called LTUF, LPUCF and LPTUF load cycles were done, these are shown in Figure 3.7, Figure 3.8 and Figure 3.9 respectively.

The LTUF load cycles were conducted so that they could be compared with the LUCF load cycles. This way path dependence, if any exists, could be detected. The LPUCF load cycles were conducted to compare the influence of each mechanism. Furthermore, LPTUF load cycles were conducted to further investigate path dependence. The LPUCF and LPTUF load cycles were conducted with A/B (J_{prel}=21 kN/m) and C/D (J_{prel}=105 kN/m) as preload level.

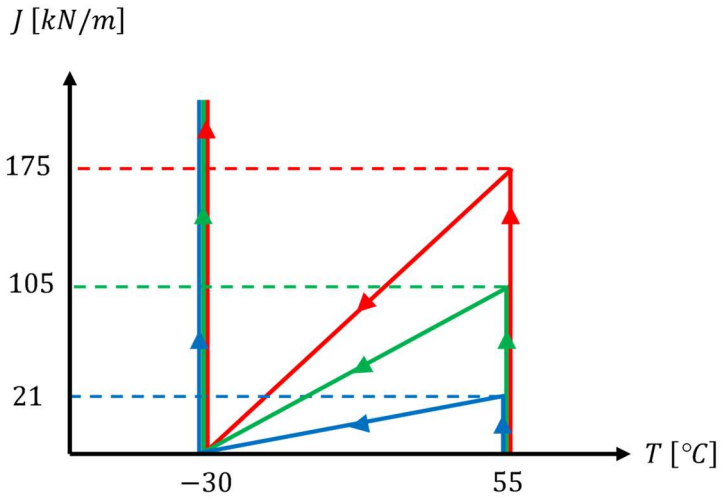

Figure 3.7. The Load-Transient-Unload-Fracture (LTUF) load cycles.

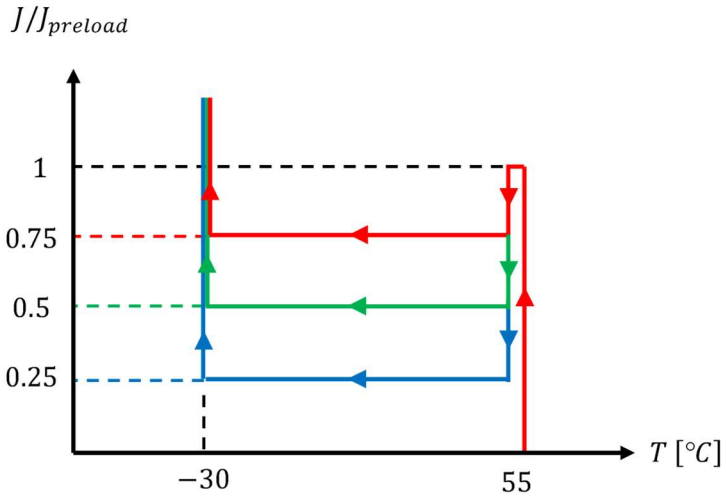

Figure 3.8. The Load-Partial-Unload-Cool-Fracture (LPUCF) load cycles.

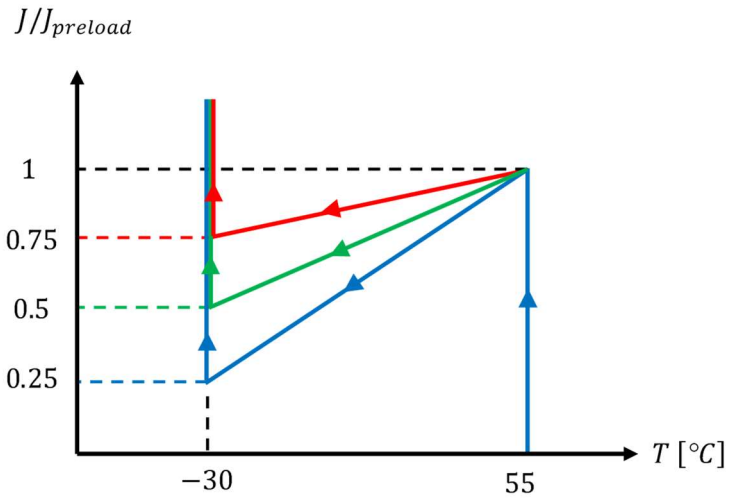

Figure 3.9. The Load-Partial-Transient-Unload-Fracture (LPTUF) load cycle.

3.4. Numerical results

To present and evaluate the results from the calibration the *J*-integral was used. The *J*-integral was evaluated using a contour integral [20] with enough contours to achieve path-independence. The *J*-integral value chosen to represent the load level was then taken as an average of the *J*-integral values along the crack front evaluated from the finite element model.

In load cases with a load history, for example the LUCF load cycle, a residual stress field will be present which means that the *J*-integral will become path dependent. To avoid incorrect *J*-integral values the probability of failure evaluated from these load cases will be plotted against the applied force divided by the limit load. This was done for all models used to evaluate the WPS mechanisms.

In the SEN(B) finite element models used for calibration of model parameters, effects from large deformations and finite strains were accounted for in a standard manner as in Kroon et al. [18]. This means that the sharp crack tip will blunt as the load is increased. As mentioned in Chapter 2.2.4 this is one of the WPS mechanisms. However, in the numerical work to evaluate the WPS mechanisms, effects from large deformations and finite strains were not accounted for. Hence, the effect of blunting will not be considered in the numerical work. This was intentional since the aim of the numerical work was to evaluate the mechanisms related to the introduction of a beneficial compressive residual stress field and the change of material properties due to the lowering of the temperature.

3.4.1. Calibration

The calibration was done on both the deeply cracked and the shallowly cracked finite element models. The material parameters for the probabilistic model were calibrated using the experimental results given in work conducted by Kroon et al. [18] for temperature equal to $-30°C$. In Figure 3.10 some of the cumulative distribution functions generated by the post-processing script during the calibration are shown as well as the optimal values of σ_{th} and c for the given value of L. These parameter values were then used in the post-processing script to generate the cumulative distribution functions for the finite element model with a crack to width ratio of 0.25 and the results are shown in Figure 3.11.

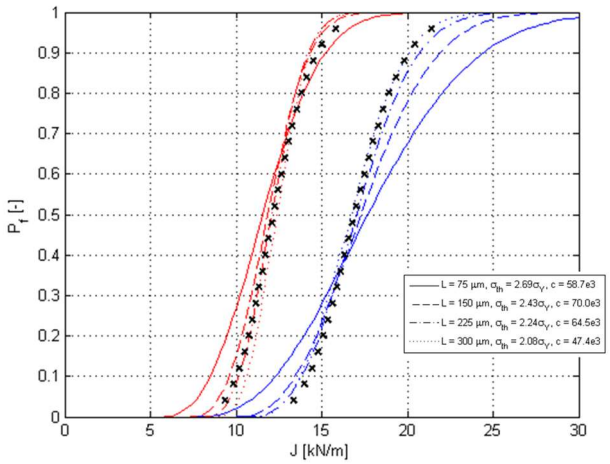

Figure 3.10. Cumulative distribution functions belonging to the two models used for parameter calibration: Deeply cracked SEN(B), with a crack to width ratio of 0.5, which is represented with red lines and shallowly cracked SEN(B), with a crack to width ratio of 0.1, which is represented with blue lines. The crosses represent the log-normal function created by experimental data.

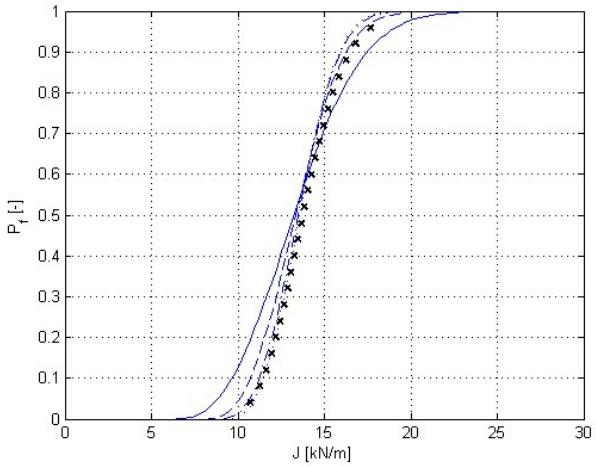

Figure 3.11. Cumulative distribution functions for model with a crack to width ratio of 0.25. The crosses represent the log-normal function created by the experimental data. The lines have the same parameters as shown in Figure 3.10.

From the results presented in Figure 3.10 and Figure 3.11 it can be seen that the post-processing script is working as intended. From the calibration the material parameters for the probabilistic model were determined to be $L = 225\ \mu m$, $\sigma_{th} = 2.24\sigma_Y$ and $c = 64.5e3$. It should be noted that the material parameters obtained in this work differs from the material parameters obtained by Kroon et al [18]. This is due to a different choice of V_0 but has not been investigated further.

3.4.2. WPS load cycles

The cumulative distribution functions for each load cycle described in Chapter 3.3.2 will be shown in this section. As previously mentioned in Chapter 3.3.2 these graphs will have the applied force (P) divided by the limit load (P_L) on the x-axis instead of the *J*-integral. Furthermore, the cumulative distribution functions are always calculated from the reloading phase at $-30\ °C$. The upwards-pointing triangle represents 95% probability of cleavage fracture, the square represents 50%, and the downwards-pointing triangle represents 5%. Furthermore, there is a cross at the end of all load cycles indicating 99.9% probability of failure. All models were preloaded at $55°C$ and reloaded at $-30°C$. But to illustrate all load cycles in the same graph, the temperature in which the models were preloaded as well as reloaded are slightly shifted in the load cycle graphs.

The Load-Cool-Fracture (LCF) load cycles are shown in Figure 3.12. The Load-Unload-Cool-Fracture (LUCF) load cycles are shown in Figure 3.13. The Load-Transient-Unload-Fracture (LTUF) load cycles are shown in Figure 3.14. In all figures the isothermal, CF, load case is viewed (with black lines) as a reference case without the influence of WPS effects.

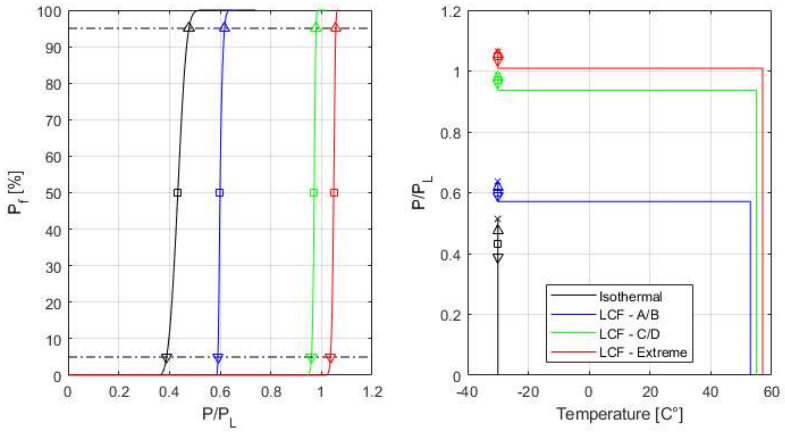

Figure 3.12. The Load-Cool-Fracture (LCF) load cycles with the cumulative distribution functions are shown in the graph to the left and the load cycles in the graph to the right.

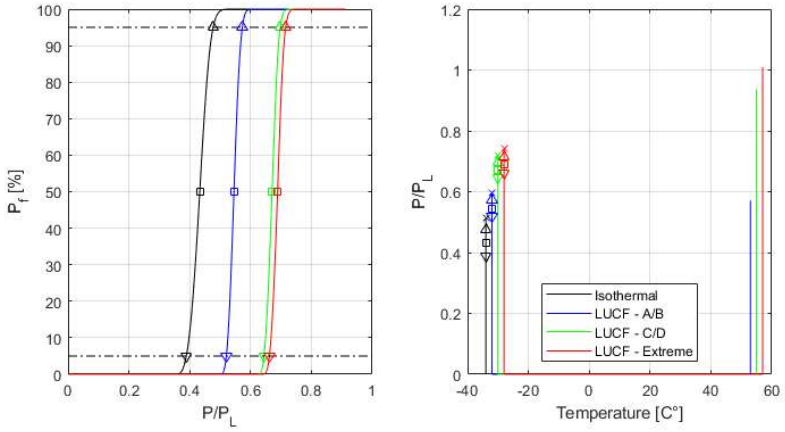

Figure 3.13. The Load-Unload-Cool-Fracture (LUCF) load cycles with the cumulative distribution functions are shown in the graph to the left and the load cycles in the graph to the right.

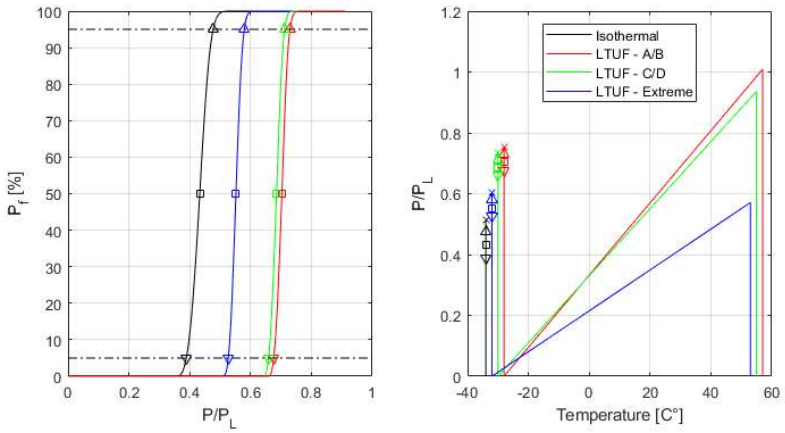

Figure 3.14. The Load-Transient-Unload-Fracture (LTUF) load cycles with the cumulative distribution functions are shown in the graph to the left and the load cycles in the graph to the right.

The results presented in Figure 3.12 show that the expected value of fracture is greatly increased by the LCF load cycle. Furthermore, the standard deviations are also lowered as a result of the LCF load cycles.

The results presented in Figure 3.13 show that the LUCF load cycle also increases the expected value of fracture as the LCF load cycle but the distance between the upwards pointing triangle and the downwards pointing triangle, i.e. the scatter, is only slightly reduced. The result for the LUCF load cycle with a preload of level $J = 21\ kN/m$ (A/B) is very similar to the experimental result obtained by Smith et al. [9]. In Smith's experiment a slightly higher preload level was used.

It can be observed from Figure 3.14 that the cumulative distribution function for the LTUF load cycle is very similar to the cumulative distribution function for the LUCF load cycle. In Figure 3.15 the differences between LUCF and LTUF load cycles are shown. It can be seen from this figure that there is a slight difference in the expected value. The expected value is slightly increased by the LTUF load cycles

compared to the LUCF load cycles. This is due to differences in the yield strength during the unloading between the LUCF and LTUF load cycles. Therefore, a slightly different residual stress field is obtained when unloading while simultaneously reducing the temperature compared to unloading for a fixed temperature.

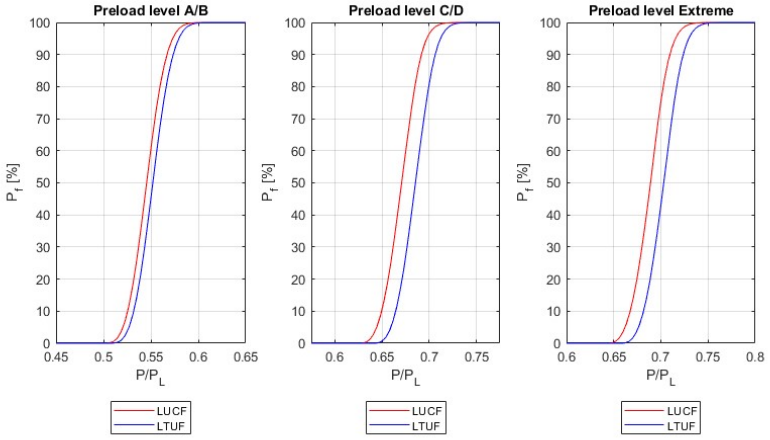

Figure 3.15. Three graphs showing the cumulative distribution function for both LUCF and LTUF load cycles at different preload levels.

The Load-Partial-Unload-Cool-Fracture (LPUCF) and Load-Partial-Transient-Unload-Fracture (LPTUF) load cycles are shown in Figure 3.16-Figure 3.19.

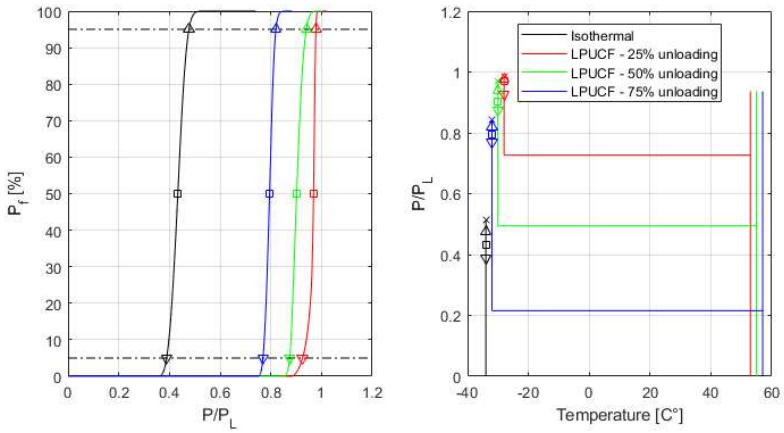

Figure 3.16. The Load-Partial-Unload-Cool-Fracture (LPUCF) load cycle with the cumulative distribution functions are shown in the graph to the left and the load cycles in the graph to the right. The preload is of level C/D (J = 105 kN/m).

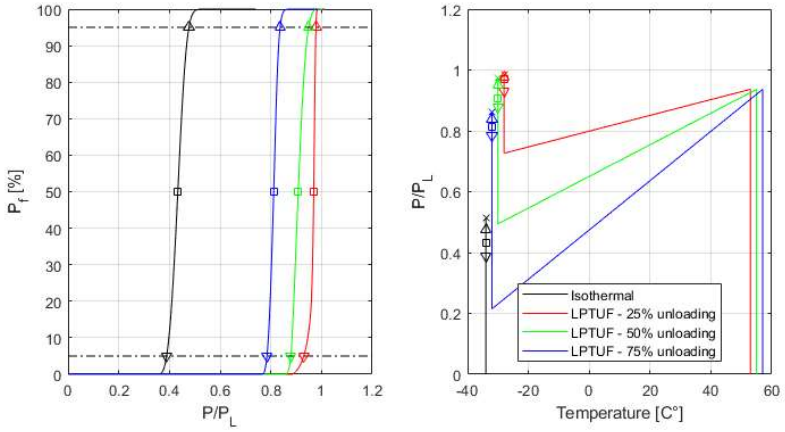

Figure 3.17. The Load-Partial-Transient-Unload-Fracture (LPTUF) load cycle with the cumulative distribution functions shown in the graph to the left and the load cycles in the graph to the right. The preload is of level C/D (J = 105 kN/m).

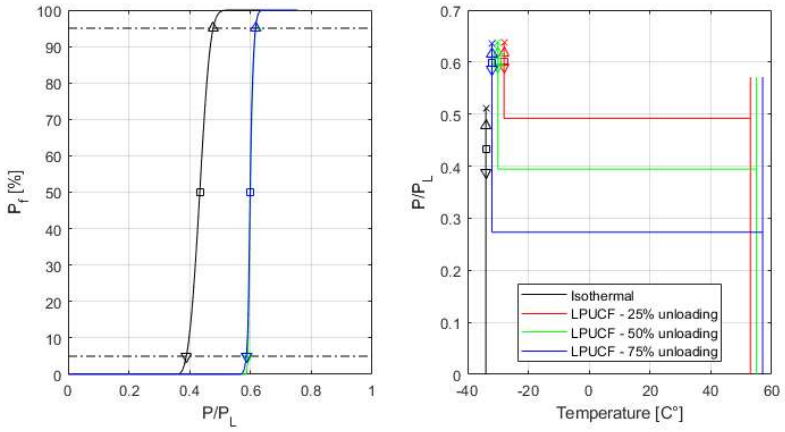

Figure 3.18. The Load-Partial-Unload-Cool-Fracture (LPUCF) load cycles with a preload level equal to A/B (J = 21 kN/m). The cumulative distribution functions are shown in the graph to the left and the load cycles in the graph to the right.

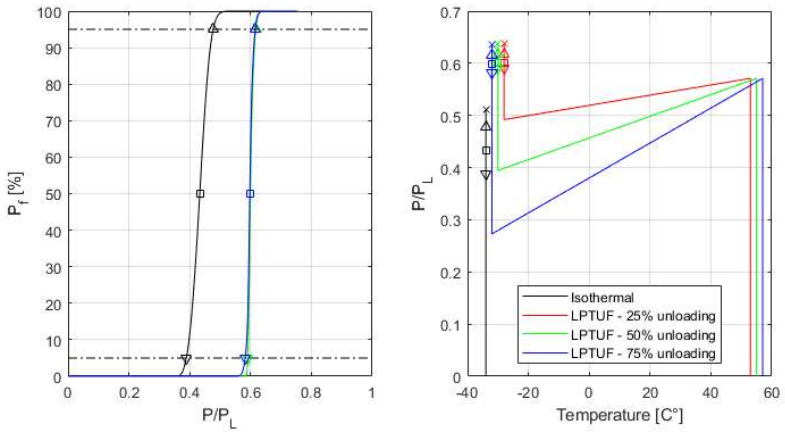

Figure 3.19. The Load-Partial-Transient-Unload-Fracture (LPTUF) load cycles with a preload level equal to A/B (J = 21 kN/m). The cumulative distribution functions are shown in the graph to the left and the load cycles in the graph to the right.

Figure 3.16 show that the expected fracture load is increased remarkably for the LPUCF load cycles with level C/D preload, similar to the increase seen in the LCF load cycles. When unloading more than 25% of the preload the distance between the upwards-pointing triangle and the downwards-pointing triangle is, however, more similar to the distances observed in the LUCF load cycles. From Figure 3.20 it can be seen that the LPUCF load cycle with a preload level of C/D is more similar to the LCF load cycle than the LUCF load cycle even when approximately 50% of the preload has been unloaded.

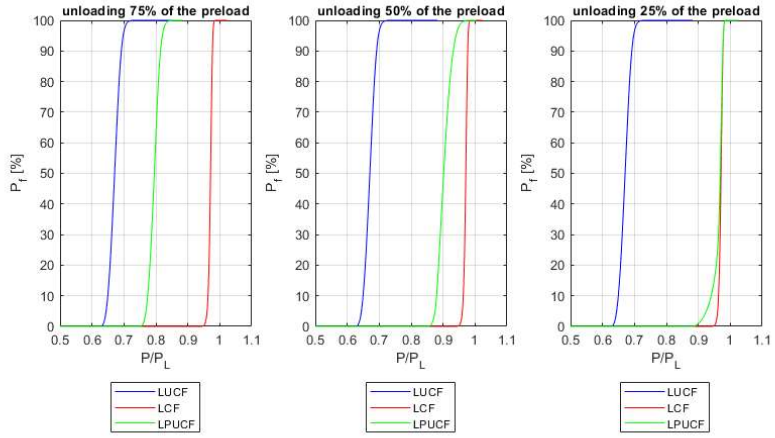

Figure 3.20. This figure compares the LUCF and the LCF load cycles with a preload level of C/D (J = 105 kN/m) to the three different LPUCF load cycles with a preload level of C/D (J = 105 kN/m).

Figure 3.17 show similar result as Figure 3.16. In Figure 3.21 below the results from Figure 3.16 and Figure 3.17 are compared as can be seen a slight difference is visible. When only 25% of the preload is unloaded

the difference between LPTUF and LPUCF takes a different shape. The expected value remains unchanged, but the lower tail still differs.

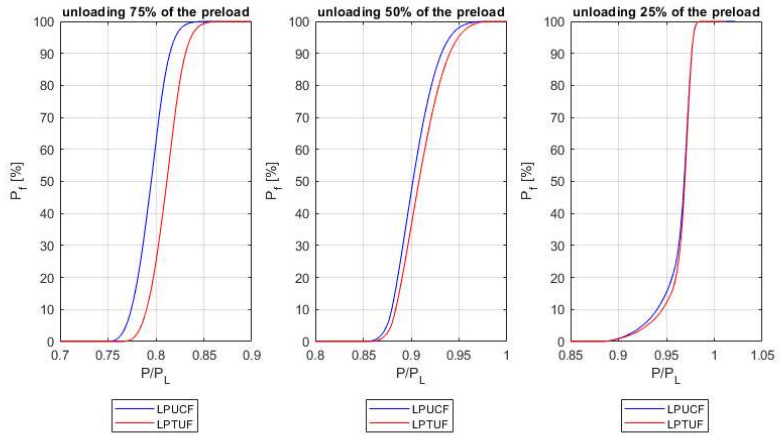

Figure 3.21. This figure compares the LPUCF load cycles with the LPTUF load cycles. The preload level of all graphs in this figure is C/D (J = 105 kN/m).

From Figure 3.18 and Figure 3.19 it can be seen that partial unloading and partial transient unloading from load level A/B neither changes the expected value nor the standard deviation. The reason for this may be that the plastic zone around the macroscopic crack tip is still relatively small. There is no significant residual stress field around the crack tip unless the entire load is removed and even then, the size of the residual stress field is relatively small. From Figure 3.22 it can be seen that the LPUCF load cycles is very similar to the LCF load cycle almost independent of the partial unloading. Only when 75% of the preload is unloaded is there a visible difference in the lower tail between the LPUCF load cycle and the LCF load cycle. From Figure 3.23 it can be seen that the partial unloading from a preload level equal to A/B appears to be path independent. Only at 75% unloading does a slight difference become visible.

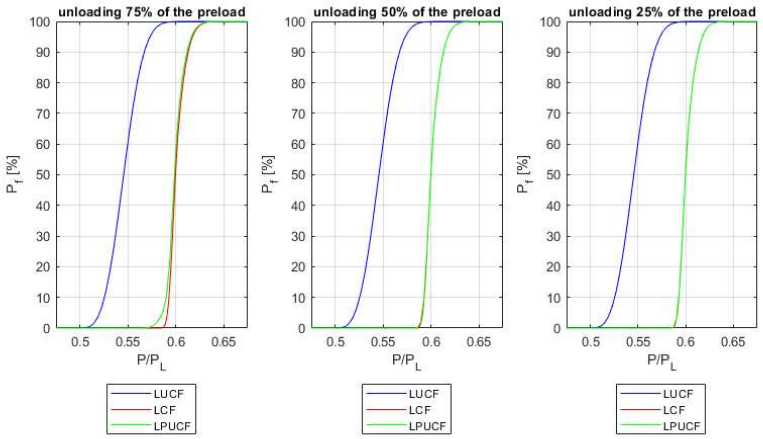

Figure 3.22. This figure compares the LUCF and the LCF load cycles with a preload level of A/B (J = 21 kN/m) to the three different LPUCF load cycles from.

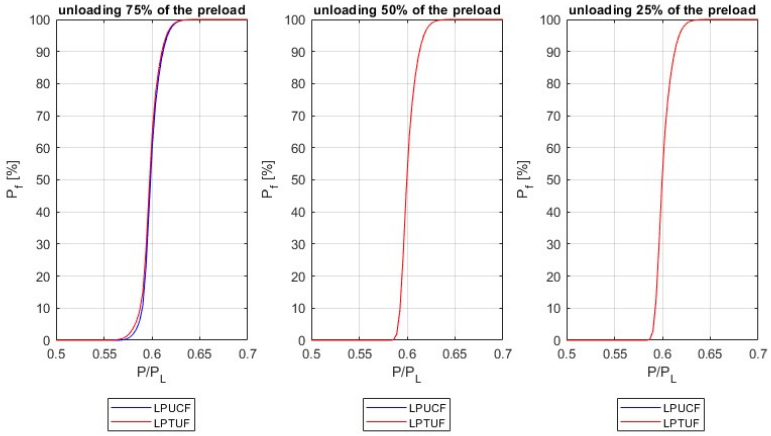

Figure 3.23. This figure compares the LPUCF load cycles to the LPTUF load cycles. The preload level of all load cycles is equal to A/B (J = 21 kN/m).

3.5. Discussion on numerical results

It should be noted that the mechanisms related to deactivation and blunting was not taken into consideration. That means that the figures used to compare the load cycles are only comparing the mechanisms related to the introduction of a beneficial compressive residual stress field and the change of material properties due to the lowering of temperature.

The LCF load cycle greatly increases the expected value of cleavage fracture and reduces the spread. The LUCF load cycle also increases the expected value of cleavage fracture but not to the same extent as the LCF load cycle. This means that the LCF load cycle is the most beneficial load cycle and thus also that the "change of material properties" mechanism is the most beneficial mechanism.

From Figure 3.15 it can be seen that the different load paths for LUCF and LTUF have a small influence on the results. Hence, the LUCF load cycle can be considered path independent during the unloading/cooling phase assuming that the load is not increased during cooling and that the yield strength is the only material property that changes with temperature.

Partial unloading of the preload, with a preload level of C/D, yields results very similar to the LCF load cycle, with equivalent preload level, even when approximately 50% of the *J*-integral value has been unloaded. Partial unloading of the preload, with a preload level of A/B, yields results almost equivalent to the LCF load cycle, with equivalent preload level, even as approximately 75% of the *J*-integral value is unloaded.

For a realistic load path, as the example in Figure 2.8 which resembles a pre-load level of A/B followed by a 75 % partial unloading, it can be concluded from the discussion above that the most influenceable mechanism, of the two studied, is the change of yield strength. Furthermore, the actual load path can be considered path independent during the unloading/cooling phase assuming that the load is not increased during cooling.

4. Experimental Work

All the experiments were conducted at the department of solid mechanics at The Royal Institute of Technology in Stockholm (KTH). The experimental program was not aimed at proving the WPS effect since there is already extensive work on this topic as has been pointed out earlier in the report. However, there is a need to thoroughly evaluate the importance of all the mechanisms behind WPS in order to understand the limitations and possibilities in using the WPS effect in assessments. Very little is known about how big of an impact the deactivation of initiation sites has on the WPS effect. The goal with the experimental work was to isolate this effect and assess its importance. It should also be mentioned that the effect of blunting and the introduction of a compressive residual stress field were also studied experimentally.

4.1. Experimental setup

The experimental program consisted of a total of 9 groups of 7 specimens each giving a total of 63 performed tests. Each individual test group had a specific setup as is outlined in Figure 4.1.

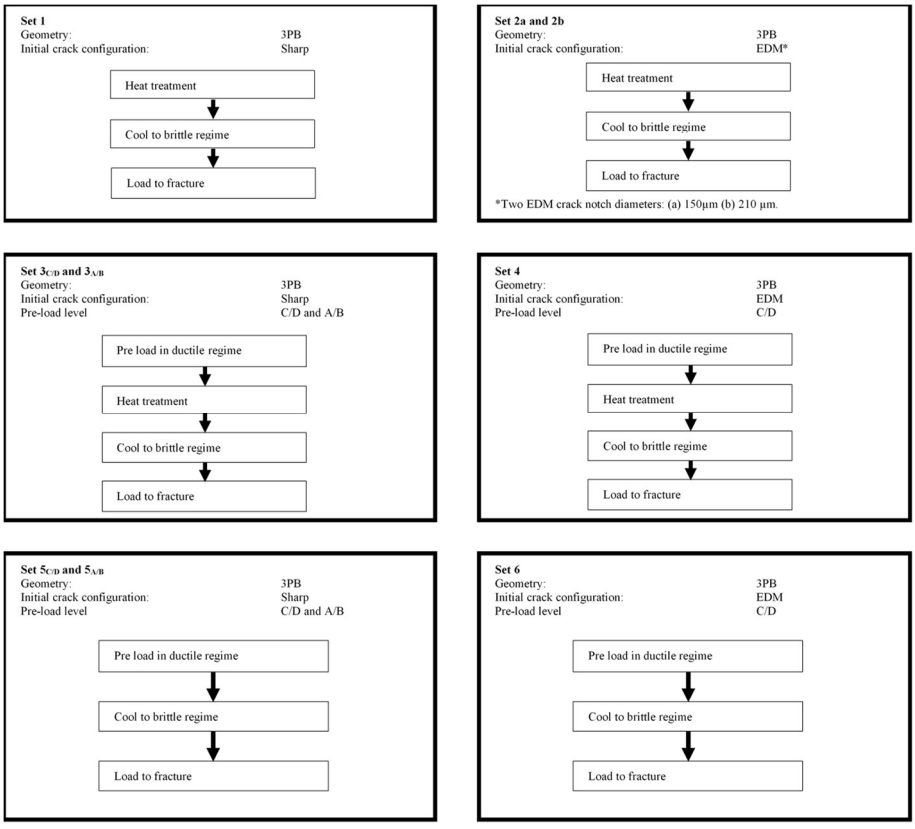

Figure 4.1. Outline of the test program and the setup for each set of tests.

The test program was designed with the aim to be able to isolate the possible effect from deactivation of initiation sites and to be able to quantify its importance for the WPS effect. Below each set will briefly be described, which WPS mechanisms are active and the purpose with the set:

Set 1

Active WPS mechanisms:	None
Purpose:	Reference case with no active mechanism to be used in comparison with other sets

Set 2a

Active WPS mechanisms:	Blunting of crack tip (EDM crack 150 µm).
Purpose:	Reference set with only the blunting mechanism. The effect of blunting was created by introducing a crack tip notch by electro discharge machining (EDM). To be compared with both Set 1 and Set 2b to evaluate the effect of blunting. To be compared with both Set $3_{A/B}$ and Set $3_{C/D}$ to evaluate the existence of the deactivation mechanism.

Set 2b

Active WPS mechanisms:	Blunting of crack tip (EDM crack 210 µm).
Purpose:	Reference set with only the blunting mechanism. The effect of blunting was created by introducing a crack tip notch by EDM. To be compared with both Set 1 and Set 2a to evaluate the effect of blunting. To be compared with Set 4 to evaluate the existence of the deactivation mechanism. Set 2b is designed to have the same amount of blunting as Set 4 after the pre-load.

Set $3_{A/B}$

Active WPS mechanisms: Blunting of crack tip (blunted crack 12 μm) and deactivation of initiation sites.

Purpose: To be compared with both Set 1, Set 2a and Set $5_{A/B}$ to evaluate the existence of the deactivation mechanism at a pre-load corresponding to a level A/B load case. It should be noted that the blunting of the crack at this pre-load is much smaller compared to the EDM crack in reference Set 2a. Note also that the heat treatment has been done to remove the mechanism of compressive residual stresses.

Set $3_{C/D}$

Active WPS mechanisms: Blunting of crack tip (blunted crack 70 μm) and deactivation of initiation sites.

Purpose: To be compared with both Set 1, Set 2a and Set $5_{C/D}$ to evaluate the existence of the deactivation mechanism at a pre-load corresponding to a level C/D load case. It should be noted that the blunting of the crack at this pre-load is smaller compared to the EDM crack in reference Set 2a. Note also that the heat treatment has been done to remove the mechanism of compressive residual stresses.

Set 4

Active WPS mechanisms: Blunting of crack tip (blunted EDM crack 210 μm) and deactivation of initiation sites.

Purpose: To be compared with both Set 1, Set 2b and Set 6 to evaluate the existence of the deactivation mechanism. It should be noted that the size of the blunted EDM crack for this Set 4 is the same as the EDM crack in Set 2b and the blunted EDM crack in Set 6. Note also that the heat treatment has been done to remove the mechanism of compressive residual stresses.

Set $5_{A/B}$

Active WPS mechanisms:	Blunting of crack tip (blunted crack 12 µm), deactivation of initiation sites and compressive residual stress field.
Purpose:	Reference set representing the full WPS effect for a LUCF load path. To be compared with both Set 1, Set 2a and Set $3_{A/B}$ to evaluate the existence of the deactivation mechanism at a pre-load corresponding to a level A/B load case. It should be noted that the blunting of the crack at this pre-load is much smaller compared to the EDM crack in reference Set 2a.

Set $5_{C/D}$

Active WPS mechanisms:	Blunting of crack tip (blunted crack 70 µm), deactivation of initiation sites and compressive residual stress field.
Purpose:	Reference set representing the full WPS effect for a LUCF load path. To be compared with both Set 1, Set 2a and Set $3_{C/D}$ to evaluate the existence of the deactivation mechanism at a pre-load corresponding to a level C/D load case. It should be noted that the blunting of the crack at this pre-load is smaller compared to the EDM crack in reference Set 2a.

Set 6

Active WPS mechanisms:	Blunting of crack tip (blunted EDM crack 210 µm), deactivation of initiation sites and compressive residual stress field.
Purpose:	Reference set representing the full WPS effect for a LUCF load path. To be compared with both Set 1, Set 2b and Set 4 to evaluate the existence of the deactivation mechanism. It should be noted that the size of the blunted EDM crack for this Set 6 is the same as the EDM crack in Set 2b and the blunted EDM crack in Set 4.

In the following chapters more information on the material, geometry, load cycles and heat treatment will be given.

4.1.1. Material

The material used in the test program was the ferritic reactor pressure vessel steel 18MND5 which was supplied by EDF France. The material has earlier been used in several research project related to WPS as for example the European research project NESC VII [12]. This made the material very suitable since it had been thoroughly characterized and a lot of data on the material was available. It was also a relevant material since it was a reactor pressure vessel steel. The material was supplied as a plate with the dimensions of 1000x300 mm with a thickness of 200 mm. Fracture specimens were machined from the lower and upper quarter of the plate. Each specimen was given a number and the distribution of the specimens to each test set was randomized, except for Set 2b. Set 2b was added to the experimental program later in the project. In Figure 4.2 a schematic sketch of the placement of the specimens in the plate is given. It should be noted that the first 60 specimens were machined from the plate in the first setup additionally 10 specimens were machined in a later state for Set 2b.

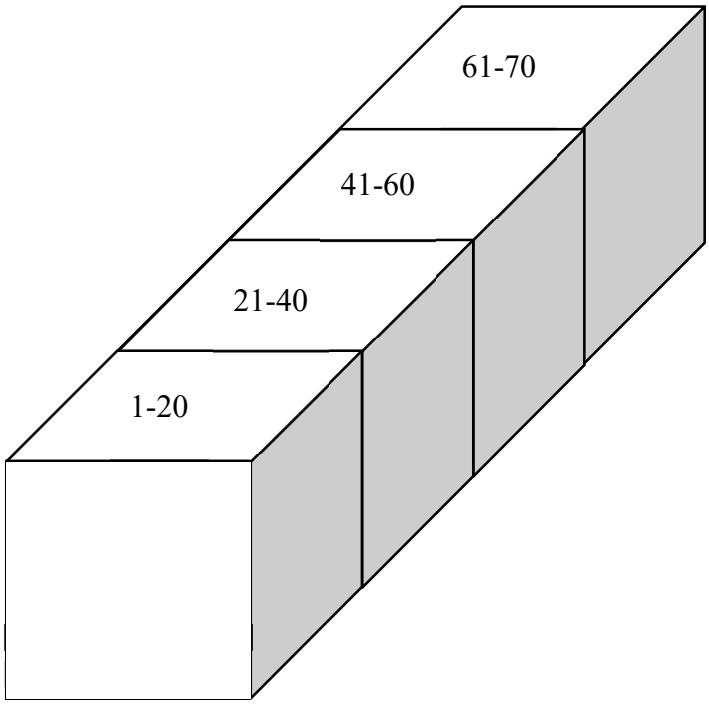

Figure 4.2. Schematic sketch of the placement of fracture specimens in the plate.

As was mentioned earlier the material had been thoroughly characterized earlier. In [12] and [14] information on the characterization of the material is given. These data are summarized here below in Figure 4.3, Table 4.1 and Table 4.2.

Table 4.1. Chemical composition of the 18MND5 steel [12].

C	Mn	Si	Ni	Cr	Mo	Cu	S	P	Al	V
0.19	1.5	0.23	0.66	0.17	0.08	0.084	<0.001	0.004	0.011	0.004

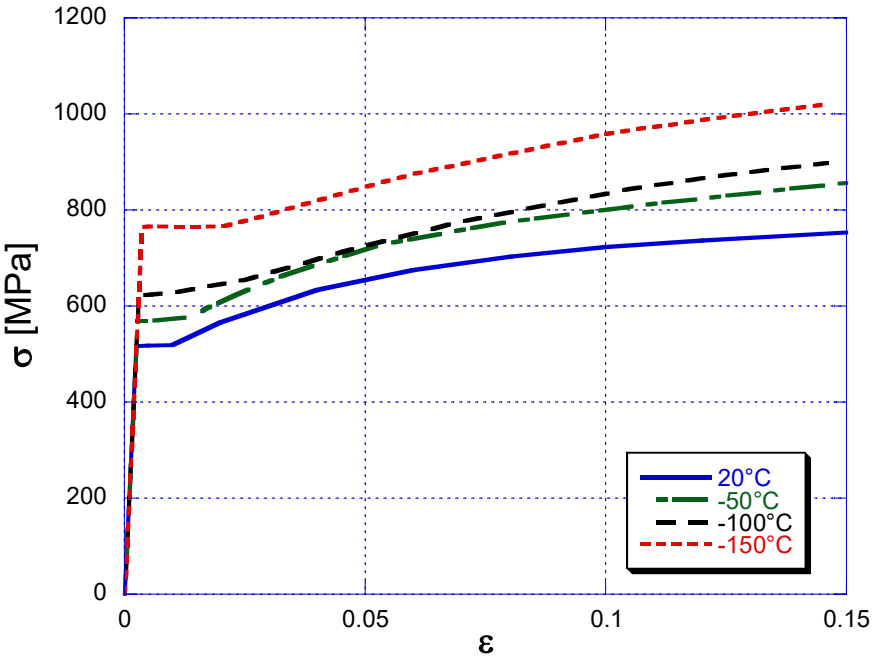

Figure 4.3. Stress-strain curves for 18MND5 ferritic steel at different temperatures [14].

Table 4.2. T_0 values for the 18MND5 steel from [12]

T_0 [°C]	
L-S orientation	L-T orientation
-98	-95

4.1.2. Test specimens

In the experimental program all tests were carried out on 3PB specimens without side grows and with W=50 mm, S=200 mm, B=25 mm and a=25 mm. In Figure 4.4 the geometry of the used 3PB specimen is shown.

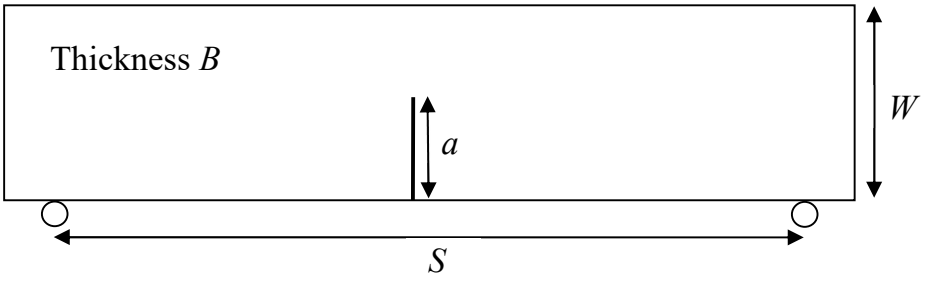

Figure 4.4. Base geometry of 3PB specimens used in the experimental program.

For Set 2a, 2b, 4 and 6 the crack was introduced only by electro discharge machining (EDM). For Set 2a, 4 and 6 a notch size of approximately 140-150 µm was machined. For Set 2b a larger notch size of approximately 210 µm was machined. In Figure 4.5. an example of two machined notches is given.

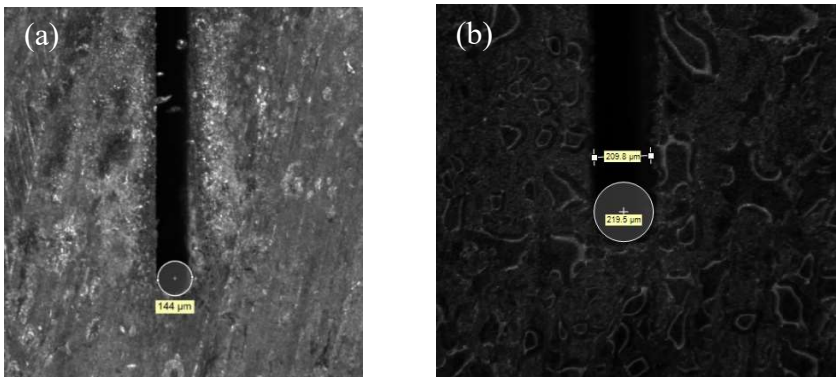

Figure 4.5. (a) EDM crack with a measured notch size of 144 µm, (b) EDM crack with a measured notch size of 219.5 µm.

For Set 1, $3_{A/B}$, $3_{C/D}$, $5_{A/B}$ and $5_{C/D}$ the crack was introduce by first EDM followed by fatigue pre-cracking creating a sharp crack.

4.1.3. Load paths

All specimens in the experimental program were loaded in three-point bending. The specimens were subjected to different load paths depending on which Set they belonged to. Three major load paths were used in the experimental program Cool-Fracture (CF), Load-Unload-Cool-Fracture (LUCF) and a variant of LUCF with a heat treatment after the pre-load. For the sets with an initially sharp fatigue crack two levels of pre-load were used for the LUCF load path. The load paths of each Set are all outlined in Figure 4.1. Below in Figure 4.6 the used load paths in the experimental program are illustrated.

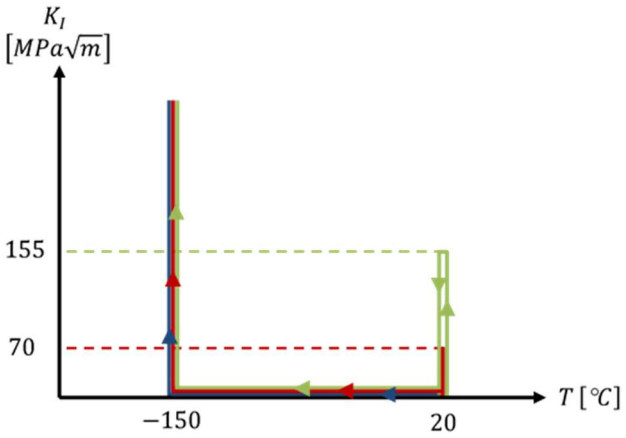

Figure 4.6. Load paths used in the experimental program, the blue line represents the CF load path, the red line represent a LUCF load path with a level A/B pre-load and the green line represents a LUCF load path with a level C/D pre-load.

For the CF load path (blue line in Figure 4.6) all specimens were cooled to -150°C before being loaded to fracture. For the LUCF load path (red and green lines in Figure 4.6) all specimens were pre-loaded at room temperature. After the pre-load the specimens were cooled to -150°C before being reloaded to fracture. The specimens belonging to Set $3_{A/B}$, $3_{C/D}$ and 4 were subjected to a heat treatment before being cooled to -150 °C. The heat treatment was done to remove the compressive residual stresses introduced by the pre-load. The heat treatment will be explained more thoroughly below in Chapter 4.1.4. Two pre-load levels were used corresponding to a level A/B load case (K_I=70 MPa√m) and C/D load case (K_I=155 MPa√m) as defined within the nuclear industry.

4.1.4. Heat treatment

The major objective of the experimental program was to isolate the effect of deactivation of initiation sites. This is rather complicated since several mechanisms act simultaneously to give the full WPS effect. For the LUCF load case three of the four mechanisms are acting. These three are the blunting of the crack tip, introduction of a compressive residual stress field and potentially the deactivation of initiation sites. The blunting of the crack tip is a geometrical change of the crack tip and is not possible to remove but the residual stresses can be reduced significantly by a proper heat treatment. Therefore, two different proposals for heat treatment were specified and verified. In the verification work both FE-analyses and experiments were used. The experimental results were used in deciding the final heat treatment specification.

Two different heat treatments were evaluated. The specifications for each heat treatment are specified below:

Heat treatment 1:

- Temperature: 620 °C
- Duration: 2 h

Heat treatment 2:

- Temperature: 620 °C
- Duration: 4.5 h

The two proposed heat treatments were evaluated experimentally. The experiments were designed using FE-analyses. A total of five test specimens were created. Three of the specimens were pre-loaded in 4 point bending (4PB) and two were kept unloaded. The geometry and loading of the specimens are shown in Figure 4.7.

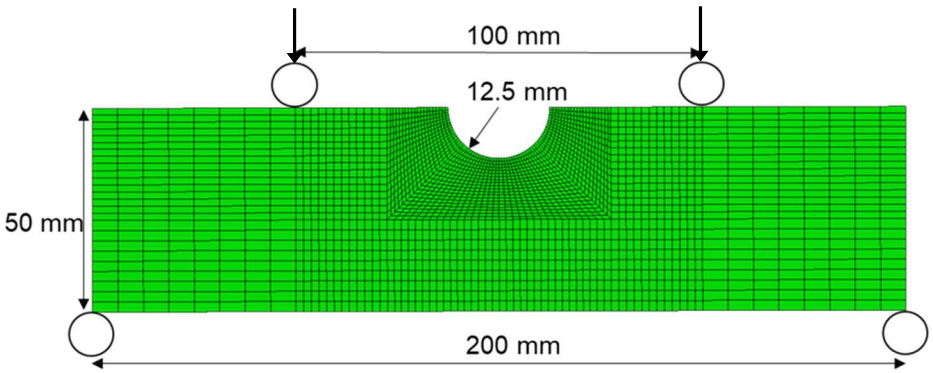

Figure 4.7. Geometry and loading of specimens used in evaluating heat treatment.

With the help of FE-analyses a pre-load was decided to 203 kN. The chosen pre-load was based on the requirement to introduce a residual stress field that was measurable. The treatment of each specimen is outlined in Table 4.3.

Table 4.3. Outline of treatment of test specimens used in evaluating the heat treatment.

Specimen	Pre-load in 4PB 203 kN	Heat treatment 1	Heat treatment 2
1	-	-	-
2	-	-	X
3	X	-	-
4	X	X	-
5	X	-	X

After each specimen had undergone the specific treatment outlined in Table 4.3. Strain gages were applied to the specimens. The placement of the strain gage was decided from FE-analyses. The strain gage was placed 11.25 mm in from the notch and offset from the symmetry line to enable the cutting as illustrated in Figure 4.8.

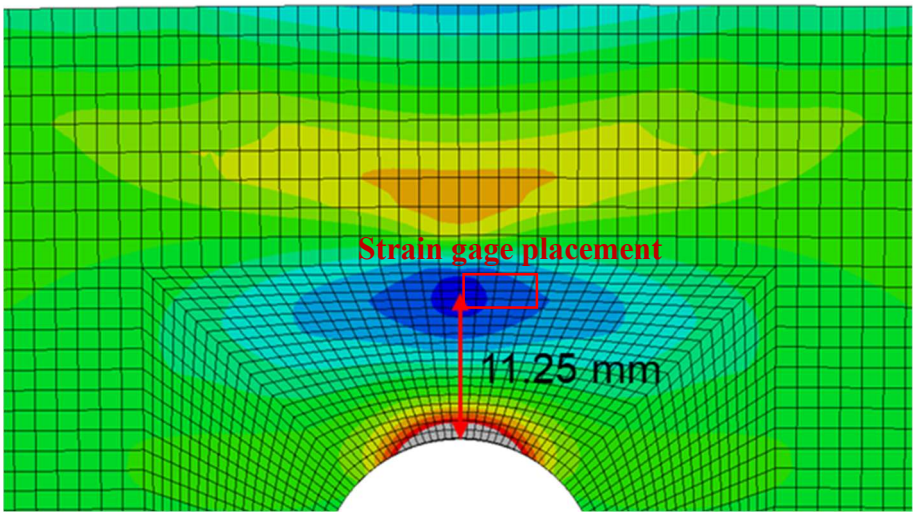

Figure 4.8. Illustration of placement of strain gage on specimen.

Thereafter the specimens were cut with EDM according to Figure 4.9 the red arrow indicates the cut. During the cutting the change in strain was measured at 3 mm cutting intervals.

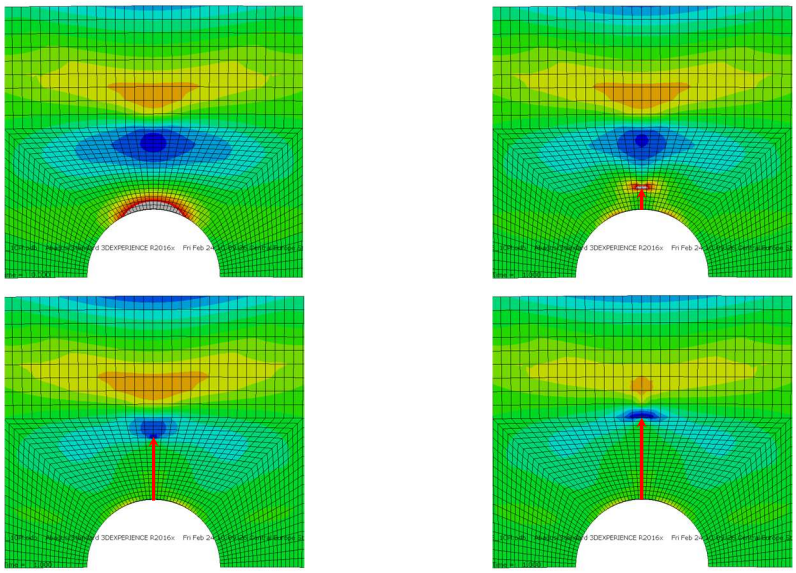

Figure 4.9. FE-analysis results illustrating the effect of cutting of pre-loaded specimen.

In Table 4.4 the results from the strain measurement are given. From these results it could be seen that a heat treatment of 620 °C in 4.5 h resulted in a reduction of the residual strains in the measured region of 94%. From the results it was decided that a heat treatment of 620 °C with a duration of 4.5 h should be used in the experimental program.

Table 4.4. Measured strains at different cutting depths.

Specimen	Strain measured at different EDM cutting depths [µm/m]					
	0 mm	3 mm	6 mm	9 mm	12 mm	15 mm
1	0	26	38	53	67	69
2	0	20	25	31	52	63
3	0	119	359	574	830	1164
4	0	27	68	121	179	333
5	0	21	40	67	81	137

4.2. Evaluation of results

During the experiments, the temperature of the specimen, load line displacement (LLD), crack mouth opening displacement (CMOD) and load was monitored. In the evaluation of the results the fracture load for each specimen was used instead of the K_I or J-integral values. The reason for this was that evaluating K_I or the J-integral using the ASTM standard in the presence of compressive residual stresses would not give correct results. Using FE-analysis and the inbuilt functions in ABAQUS would give path dependent results. Furthermore, during the project it was discovered that using the modified J-integral implemented in ABAQUS, which should be able to handle residual stresses, gave obvious erroneous results when considering compressive residual stresses. Therefore, it was decided to evaluate all experimental results using the fracture load. The experimental results presented in Chapter 4.4.1 are displayed as symbols for each individual specimen where the cumulative probability have been derived using Equation (3.14), an approximation suggested by Wallin [19]. Note that specimens are sorted from smallest to largest measured fracture load before evaluating Equation (3.14). As was stated earlier, accurate results are obtained by setting the variable C equal to 0.3 [19]. Furthermore, a fitted cumulative Weibull probability distribution was also presented with the data. The fitted curves shown in the results were created with the use of inbuilt functions within the software Matlab [21]. These functions enable a fitting of a two parameter Weibull function to a set of data points.

4.3. Fractographical examination

The fractographical examination was carried out by SINTEF in Norway. A total of 21 specimens fracture surfaces were evaluated. The specimens examined were from Set 1, $3_{C/D}$ and $5_{C/D}$. These three sets were chosen since they represented a reference case (Set 1), a set with the full WPS effect (Set $5_{C/D}$) and a set with only the blunting and deactivation mechanisms (Set $3_{C/D}$). The fracture surfaces were looked at with optical microscope and scanning electron microscope (SEM). The operator performing the fractographical examination had no prior knowledge of the project or the origin and load history of the specimens in order to minimize a biased result. The distance from the initial crack front to the initiation point was recorded for each specimen.

4.4. Experimental results

4.4.1. Experiments results

All specimens failed by cleavage fracture. Below in Table 4.5 a summary of the results from the fracture tests for each Set is presented. Figure 4.10-Figure 4.13 shows the comparisons of the different sets outlined above in Chapter 4.1.

Table 4.5. Fracture load for different probability of failure P_f=50, 95, 5% for each Set.

Set	Fracture Load [kN]		
	P_f= 5%	P_f= 50%	P_f= 95%
1	16.4	24.0	30
2a	24.6	31.8	36.9
2b	22.5	31.8	38.5
$3_{A/B}$	22.8	31.6	37.9
$3_{C/D}$	30.8	37.4	41.8
4	41.6	48.2	52.4
$5_{A/B}$	30.7	34.5	36.8
$5_{C/D}$	48.0	51.8	54.1
6	54.4	58.2	60.5

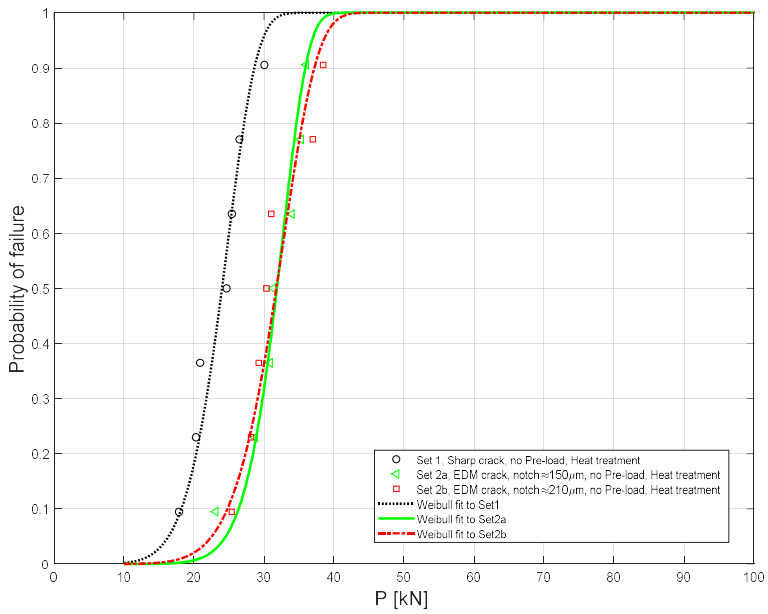

Figure 4.10. Comparison of Set1 (No WPS mechanism), Set2a (crack tip notch 150 μm) and Set2b (crack tip notch 210 μm).

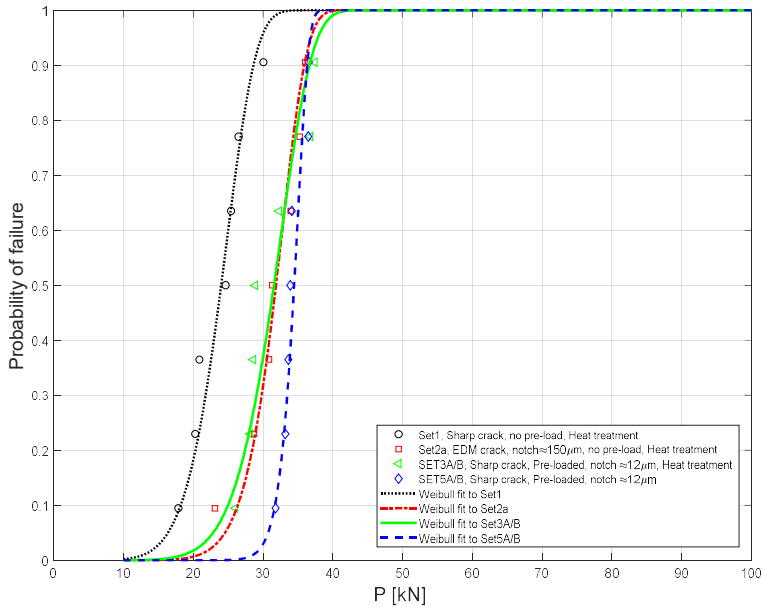

Figure 4.11. Comparison of Set1 (No WPS mechanism), Set2a (crack tip notch 150 μm), Set3$_{A/B}$ (crack tip notch 12μm and deactivation) and Set5$_{A/B}$ (crack tip notch 12μm, deactivation and residual stresses).

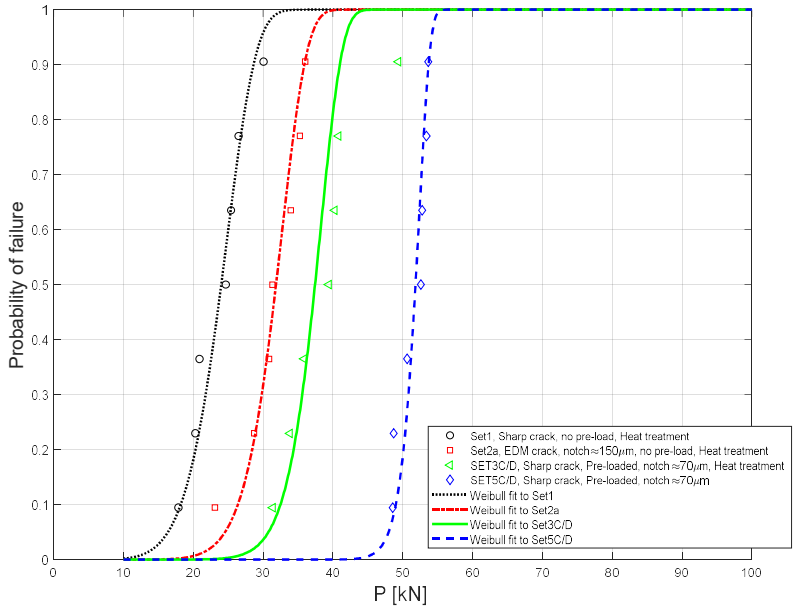

Figure 4.12. Comparison of Set1 (No WPS mechanism), Set2a (crack tip notch 150 μm), Set3$_{C/D}$ (crack tip notch 70μm and deactivation) and Set5$_{C/D}$ (crack tip notch 70μm, deactivation and residual stresses).

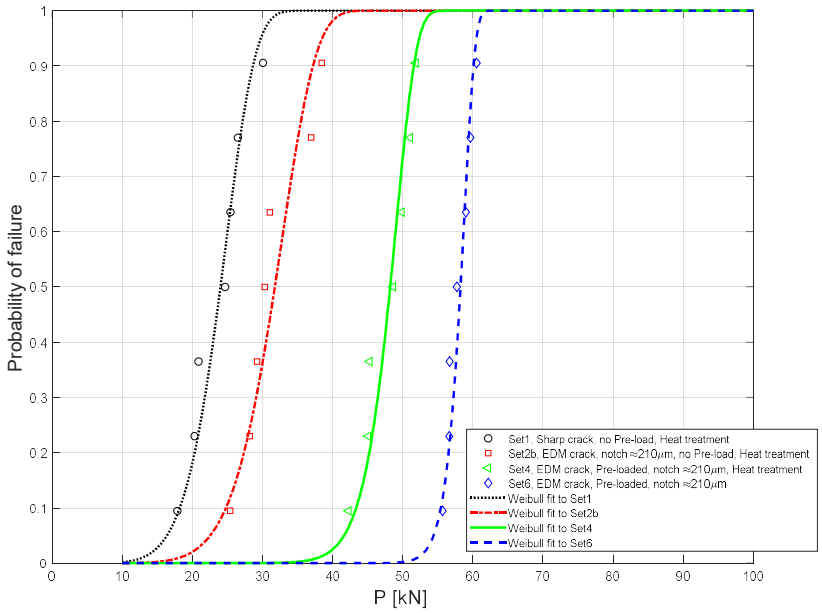

Figure 4.13. Comparison of Set1 (No WPS mechanism), Set2b (crack tip notch 210 μm), Set4 (crack tip notch 210μm and deactivation) and Set6 (crack tip notch 210μm, deactivation and residual stresses).

4.4.2. Fractographical examination

Below the results from the fractographical examination is presented. All specimens that were looked at had failed by transgranular cleavage fracture. In Figure 4.14 and Figure 4.15 the fracture surface of a specimen with and without pre-load are shown.

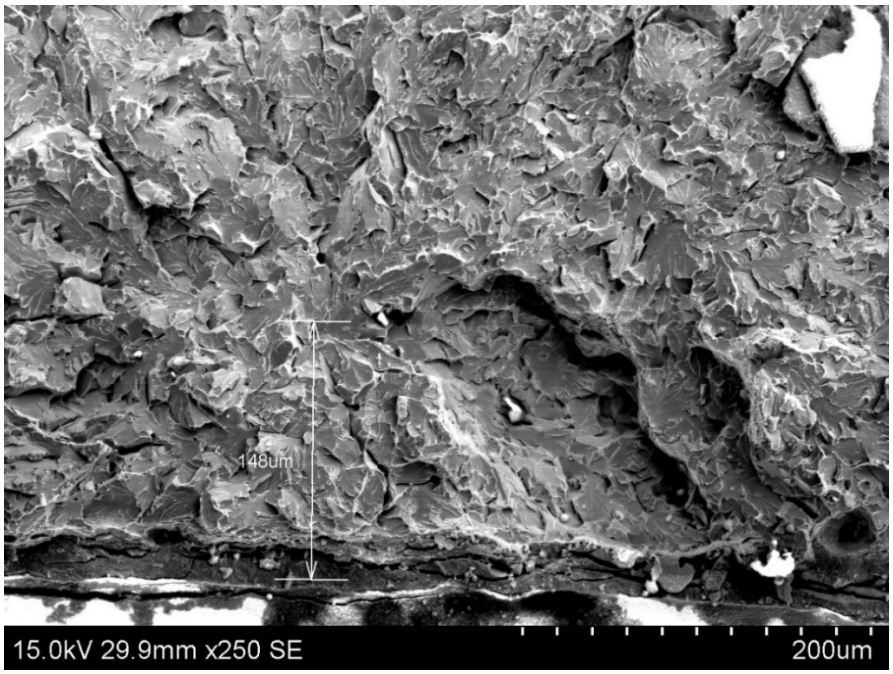

Figure 4.14. Specimen 19485 from Set3 with pre-load corresponding to a level C/D.

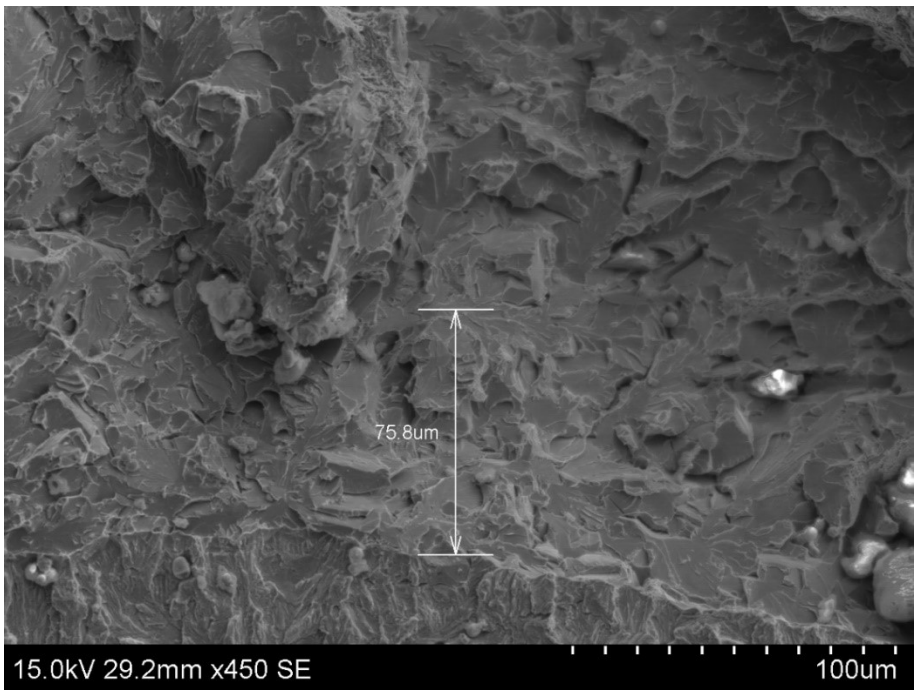

Figure 4.15. Specimen 19478 from Set1 without pre-load.

In Figure 4.16 the results from the fractographical examination for the individual specimen is plotted. The Y-axis is the fracture load and the X-axis is the distance from the initial crack front to the identified point of cleavage fracture initiation. The black circle symbols represent specimens from Set 1, the green square symbols represent specimens from Set $3_{C/D}$ and the blue triangular symbols represent specimens from Set $5_{C/D}$. In Figure 4.17 the probability density of fracture initiation in regards to distance from the crack tip is given for Set 1, Set $3_{C/D}$ and Set $5_{C/D}$. During the fractographical examination for some of the specimens that had been pre-loaded voids where found near the crack tip. In Figure 4.18 an example of this is shown.

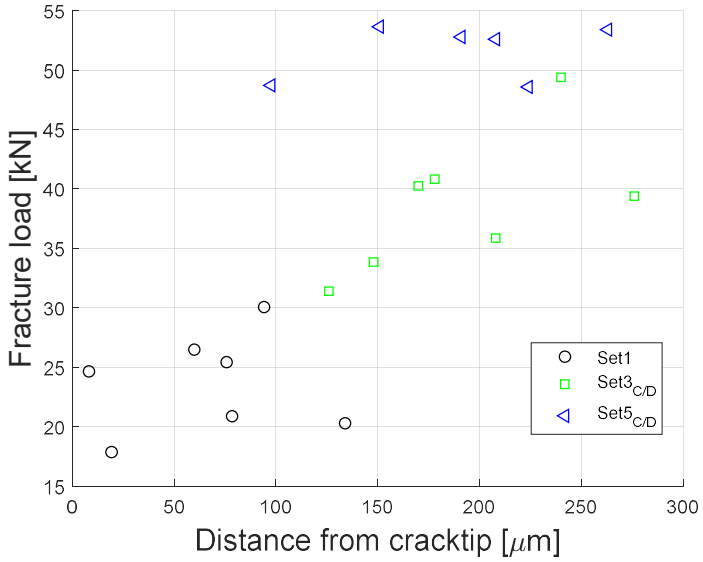

Figure 4.16. Results from fractographical examinations, distance from the crack tip for the cleavage fracture initiation sites plotted against the fracture load for each individual specimen.

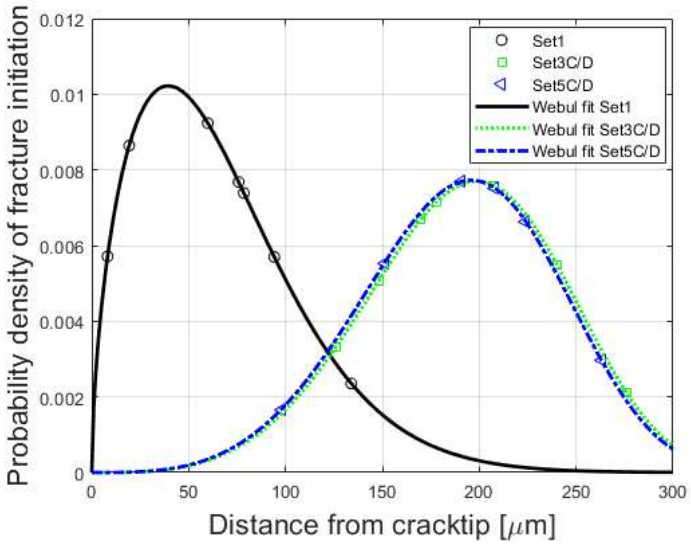

Figure 4.17. Probability density of fracture initiation in regard to distance from the crack tip for Set1, Set$3_{C/D}$ and Set$5_{C/D}$.

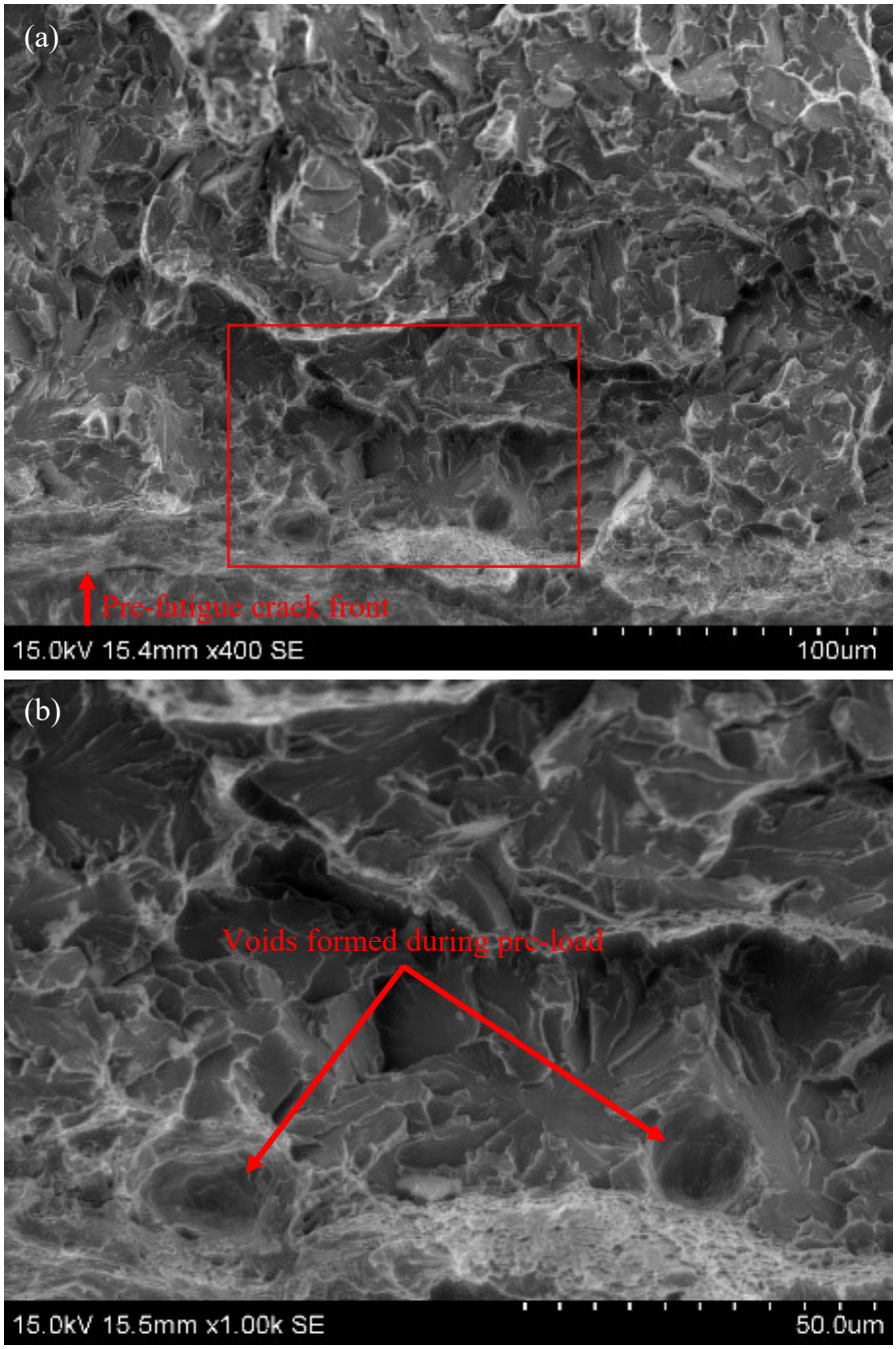

Figure 4.18. (a) SEM picture with magnification of 400 times, specimen (19491) belonging to Set5C/D. (b) Magnification of 1000 times of area marked in (a), formed voids clearly visible.

4.4.3. Discussion on experimental results

A EDM crack with a notch size over 150 µm clearly influence the fracture load as can be seen in Figure 4.10. Furthermore, it is also observed in Figure 4.10 that there is no significant difference between a EDM crack with a notch size of 150µm and 210µm. Unfortunately, at the time when the experimental work was conducted there was no possibility to create a smaller notch size by EDM. The results in Figure 4.10 suggest that there seems to be an upper bound on the effect from blunting. But further studies would be needed to confirm this. It should also be mentioned in regards to crack blunting that the influence on the fracture load is less than what is seen from the other mechanisms as can be seen in Figure 4.11-Figure 4.13.

A pre-load corresponding to a level A/B load case gives a WPS effect shown in Figure 4.11. In Figure 4.11 it can also be seen that the effect of 12µm crack blunting together with deactivation of initiation sites give very similar effect as a EDM crack of 150µm. Assuming that a crack blunting of 12 µm do not give the same effect as a EDM crack of 150 µm, the results in Figure 4.11 reveal that the deactivation of initiation sites is an active mechanism even at pre-loads corresponding to a level A/B load case. Set $5_{A/B}$ which represents the full WPS effect including compressive residual stresses still show the largest effect on the fracture load. Note that the compressive residual stresses are the mechanism contributing the most to the WPS effect for a LUCF load path.

In Figure 4.12 it is clearly shown that for a level C/D pre-load the deactivation is an active mechanism. Comparing the results from Set 2a, EDM crack of 150µm, with the results of Set $3_{C/D}$, crack blunting of 70µm and without any compressive residual stresses, it is clear that the deactivation of initiation sites is a contributing mechanism that effects and increases the fracture load. This is also very clear in Figure 4.13 where all specimen except Set1 have the same level of blunting. From Figure 4.12 and Figure 4.13 it can also be concluded that the deactivation of initiation sites have a larger effect on the fracture load compared with only the blunting of the crack tip.

The conclusions that the deactivation of initiation sites is an active mechanism for the WPS effect is reinforced by the fractographical examinations. In Figure 4.16 it is seen that for both Set $3_{C/D}$ and Set $5_{C/D}$ the position of the initiation sites are clearly affected by the pre-load even if the compressive stresses have been removed by a heat treatment. In Figure 4.17 this is also very clear. Figure 4.16 and Figure 4.17 show that the positions of the initiations sites for Set $3_{C/D}$ and Set $5_{C/D}$ is not influenced by the difference in fracture load that is due to the compressive residual stresses for Set $5_{C/D}$. Hence, the clear alternation of the positioning of the initiation sites in Set $3_{C/D}$ and Set $5_{C/D}$ compared to Set 1 is due to the deactivation of initiation sites near the crack tip. Furthermore, during the fractographic examination voids that had been formed during the pre-loading were found, see Figure 4.18.

5. Conclusions

From the numerical and experimental results presented in this report the main conclusions are:

- For a realistic load case, shown in Figure 2.8, the most influential mechanism behind the WPS effect is the change in yield strength due to the lowering of the temperature. Furthermore, the actual load path can be considered path independent during the unloading/cooling phase assuming that the load is not increased during cooling (monotonous decline).
- The results also clearly show that for a realistic load case, as shown in Figure 2.8, the deactivation of initiation sites is an active and significant mechanism.
- The experimental results show that the deactivation of initiation sites is an active mechanism for pre-loads corresponding to a level A/B load case and higher pre-loads.
- Comparing the LUCF and LCF load path effects, it is shown that the LCF load path is the most beneficial. Hence, the change of yield strength mechanism is the most beneficial mechanism.

Furthermore, the following can be concluded from the numerical and experimental results:

- The LUCF load cycle can be considered path independent during the unloading/cooling phase assuming a total unloading.
- Partial unloading of the preload, with a preload level of C/D, yields results very similar to the LCF load cycle, with equivalent preload level, even when approximately 50% of the J-integral value has been unloaded.
- Partial unloading of the preload, with a preload level of A/B, yields results almost equivalent to the LCF load cycle, with equivalent preload level, even as approximately 75% of the J-integral value is unloaded.
- A EDM crack with a notch size >150 μm clearly influences the fracture load. But it should also be mentioned that the influence on the fracture load is less than what is seen from the other mechanisms that have been examined.
- The deactivation of initiation sites has a larger effect on the fracture load compared with only the blunting of the crack tip.
- The positions of the initiation sites for pre-loaded specimens with and without compressive residual stresses is not influenced by the difference in fracture load that is due to the compressive residual stresses.

6. Need for further research

Even though work on the WPS effect have been done since the 70:s there are still gaps in the knowledge about the WPS effect and it's use for real components during realistic loading transients. One of these gaps is what the margin to fracture is during the cooling for a load transient.

In theory, a component would not fracture when the load is held constant during the cooling. But there is no knowledge of what the margin to fracture is. There are published experiments [11] where specimens subjected to a Load-Cool-Fracture (LCF) transient have experienced fracture during the cooling sequence where the load is to be held constant. At the same time there are other published experiments [22] where an increasing load has been applied during the cooling where fracture has not occurred. Hence, there seems to be a significant scatter in the level of margin during the cooling. This also justifies the need to evaluate the margins to fracture during a loading transient.

The effect from a residual stress field on the WPS effect is also important to understand since defect are usually found in welds. There is very little published work on this subject though. Therefore, an experimental program to look at the effect on the interaction between a prior residual stress field and the WPS effect would be valuable. This could also be strengthened by a numerical study to advance the understanding even further of the interaction between a prior residual stress field and the WPS effect.

7. Acknowledgement

The authors are grateful for the financial support of The Swedish Radiation Safety Authority and NKS. The authors would also like to thank EDF France for assisting in supplying the material used in the experiments. A special thanks to Dominique Moinereau at EDF France who greatly helped in acquiring the material.

8. References

[1] M. Kroon och J. Faleskog, ”A probabilistic model for cleavage fracture with a length scale - influence of material parameters and constraint,” *International Journal of Fracture,* vol. 118, pp. 99-118, 2002.

[2] C. J. McMahon och M. Cohen, ”Initiation of cleavage in polycrystalline iron,” *Acta metallurgica ,* vol. 13, 1965.

[3] M. Stec, ”Micromechanical modeling of cleavage fracture in polycrystalline materials, Doctoral Thesis,” Royal Institute of Technology, Engineering Sciences, Solid Mechanics, Stockholm, 2008.

[4] T. L. Anderson, Fracture Mechanics, Fundamentals and Applications, Second Edition, 1995.

[5] M. Kroon och J. Faleskog, ”Micromechanics of cleavage fracture initiation in ferritic steels by carbide cracking,” *Journal of the Mechnics anf Physics of Solids,* vol. 53, pp. 171-196, 2005.

[6] T. Lin, A. G. Evans och R. O. Ritchie, ”A statistical model of brittle fracture by transgranular cleavage,” *Journal of the Mechanics and Physics of Solids,* vol. 34, pp. 477-497, 1986.

[7] R. O. Ritchie, J. F. Knott och J. R. Rice, ”On the relationship between critical tensile stress and fracture toughness in mild steel,” *Journal of Mechanics and the Physics of Solids,* vol. 21, pp. 395-410, 1973.

[8] P. Bowen, S. G. Druce and J. F. Knott, "Micromechanical modelling of fracture toughness," *Acta metallurgica,* vol. 35, no. 7, pp. 1735-1746, 1987.

[9] D. J. Smith, S. Hadidimoud och H. Fowler, ”The effects of warm pre-stressing on cleavage fracture. Part 1: evaluation of experiments,” *Engineering Fracture Mechanics,* vol. 71, pp. 2015-2032, 2004.

[10] T. Yuritzinn, L. Ferry, S. Chapuliot, P. Mongabure, D. Moinereau, A. Dahl och P. Gilles, ”Illustration of the WPS benefit through BATMAN test series: Tests on large specimens under WPS loading configurations,” *Engineering Fracture Mechanics,* vol. 75, pp. 2191-2207, 2008.

[11] S. Chapuliot, D. Lauerova, M. Brumovsky och B. Tanguy, ”Information about WPS experiments performed in NRI REZ and their evaluation,” i *Fontevraud 7*, 2010.

[12] D. Moinereau, S. Chapuliot, S. Marie och C. Jacquemoud, ”NESC VII synthesis: A european project for application of WPS in RPV assesment including biaxial loading,” i *ASME 2014 Pressure Vessels & Piping Conference*, Anaheim, California, USA , 2014.

[13] J. D. Landes, D. E. McCabe och J. A. M. Boulet, ”Fracture Mechanics Twenty-fourth Volume,” *ASTM STP 1207,* pp. 186-207.

[14] W. Lefevre, G. Barbier, R. Masson och G. Rousserlier, ”A modified Beremin model to simulate the warm pre-stress effect,” *Nuclear Engineering and Design,* vol. 216, pp. 27-42, 2002.

[15] F. M. Beremin, ”A local criterion for cleavage fracture of a nuclear pressure vessel steel,” *Metallurgical Transactions A,* vol. 14A, pp. 2277-2287, 1983.

[16] J. Gurland, ”Obesrvation on the fracture of cementite particles in a spheroidized 1.05% C steel deformed at room temperature,” *Acta Metallurgica,* vol. 20, 1972.

[17] S. Lee, S. Kim, B. Hwang, B. S. Lee och C. G. Lee, ”Effect of carbide distribution on the fracture toughness in the transition temperature region of an SA 508 steel,” *Acta Materialia,* vol. 50, pp. 4755-4762, 2002.

[18] M. Kroon, J. Faleskog och H. Öberg, ”A probabilistic model for cleavage fracture with a length scale - parameter estimation and predictions of stationary crack experiments,” *Engineering Fracture Mechanics,* vol. 71, pp. 57-79, 2004.

[19] K. Wallin, ”Statistical aspects of constraint with emphasis on testing and analysis of laboratory specimens in the transition region,” *ASTM STP,* vol. 1171, pp. 264-288, 1993.

[20] Hibbit, Karlsson och Sorenson, ”ABAQUS Version 6.14 Documentation”.

[21] ”Matlab R2018b, Statistics and Machine Learning Toolbox,” The MathWorks, Inc, 2018.

[22] S. R. Bordet, B. Tanguy, J. Besson, S. Bugat, D. Moinereau och A. Pineau, ”Cleavage fracture of RPV steel following warm pre-stressing: micromechanical analysis and interpretation through a new model,” *Fatigue Fract Engng Mater Struct,* vol. 29, pp. 799-816, 2006.

The Swedish Radiation Safety Authority has a comprehensive responsibility to ensure that society is safe from the effects of radiation. The Authority works from the effects of radiation. The Authority works to achieve radiation safety in a number of areas: nuclear power, medical care as well as commercial products and services. The Authority also works to achieve protection from natural radiation an to increase the level of ratiation safety internationally.

The Swedish Radiation Safety Authority works proactively and presentively to protect people and the environment from the harmful effects of radiation, now and in the future.
The Authority issues regulations and supervises compliance, while also supporting research, providing training and information, and issuing advice. Often, activities involving radiation require licences issued by the Authority. The Swedish Radiation Safety Authority maintains emergency preparedness around the clock with the aim of limiting the aftermath of radiation accidents and the unintentional spreading of radioactive substances. The Authority participates in international co-operation in order to promote radiation safety and finances projects aiming to raise the level of radiation safety in certain Eastern European countries.

The Authority reports to the Ministry of the Environment and has around 300 employees with competencies in the fields of engineering, natural and behavioral sciences, law, economics and communications. We have recieved quality, environmental and working environment certification.

Publikationer utgivna av Strålsäkerhetsmyndigheten kan laddas ned via stralsäkerhetsmyndigheten.se eller beställas genom att skicka e-post till registrator@ssm.se om du vill ha broschyren i alternativt format, som punktskrift eller daisy.

Strålsäkerhetsmyndigheten
Swedish Radiation Safety Authority
SE-171 16 Stockholm
Phone: 08-799 40 00
Web: ssm.se
E-mail: registrator@ssm.se

E-print AB, 2022